On the Impact of Tropical Cyclones on Rossby Wave Packets: A Climatological Perspective⌀

JULIAN F. QUINTING

Institute for Meteorology and Climate Research, Karlsruhe Institute of Technology, Karlsruhe, Germany, and Institute for Atmospheric and Climate Science, ETH Zurich, Zurich, Switzerland

SARAH C. JONES

Deutscher Wetterdienst, Offenbach, Germany

ABSTRACT

Many studies have highlighted the importance of recurving tropical cyclones (TCs) in triggering Rossby waves. This study investigates the impact of western North Pacific (WNP), south Indian Ocean, and North Atlantic recurving TCs on the amplitude and frequency of synoptic-scale Rossby wave packets (RWPs) over a 30-yr period. The results indicate a significant increase of RWP frequency downstream of WNP and south Indian Ocean TCs. A statistically significant RWP amplitude anomaly downstream of these TCs suggests that RWPs, which are associated with TCs, are stronger than those that generally occur in midlatitudes. North Atlantic TCs do not seem to be associated with a statistically significant increase in RWP frequency and amplitude downstream.

Processes that contribute to Rossby wave amplification are identified by creating composites for WNP TCs with and without downstream development. Potential vorticity, eddy kinetic energy, and quasigeostrophic forcing diagnostics highlight dynamical mechanisms that contribute to the synergistic interaction between the TC and the midlatitude flow. The existence of an upstream Rossby wave favors a downstream development. Diabatically enhanced upper-level divergent flow that can be attributed to the nonlinear interaction between the TC and the midlatitude flow impedes the eastward propagation of the upstream trough, amplifies the downstream ridge, and intensifies the jet. The amplified midlatitude flow provides upper-level forcing, which helps to maintain the predominantly diabatically driven divergent flow.

Forecast uncertainties that are related to these complex TC–midlatitude flow interactions may spread into downstream regions. A climatological analysis of ensemble reforecast data emphasizes the importance of TC–midlatitude flow interactions and Rossby wave amplification on downstream predictability.

1. Introduction

Tropical cyclones (TCs) that recurve and undergo extratropical transition (ET; Jones et al. 2003) interact with the midlatitude flow and may modify the extratropical flow pattern. Numerical studies in a barotropic framework, full-physics numerical experiments, and observational case studies showed that this modification can be associated with the excitation of Rossby waves (e.g., Nieto Ferreira and Schubert 1999; Agusti-Panareda et al. 2004; Riemer et al. 2008; Harr and Dea 2009; Riemer and Jones 2010; Scheck et al. 2011a; Grams et al. 2013b). Recent climatological studies by Archambault et al. (2013, 2015) and Torn and Hakim (2015) confirmed these findings. They showed that recurving western North Pacific (WNP) and North Atlantic TCs are followed by a significant amplification of the meridional flow in downstream regions. This amplification indicates that recurving WNP TCs as well as

recurving North Atlantic TCs are associated with downstream Rossby wave dispersion.

The dispersion of Rossby waves into downstream regions has the ability to cause surface cyclogenesis (Agusti-Panareda et al. 2004; Cordeira and Bosart 2010) or high-impact weather events such as severe precipitation (e.g., Martius et al. 2008; Grams et al. 2011; Grams and Blumer 2015). Furthermore, initial perturbations and ET-related forecast uncertainties tend to grow and spread into downstream regions in connection with the development of midlatitude Rossby wave packets (RWPs) (e.g., Harr et al. 2008; Reynolds et al. 2009; Anwender et al. 2010; Pantillon et al. 2013). Hence, it is of interest to investigate the excitation and modification of Rossby waves through TCs over various ocean basins in order to quantify how and to what extent recurving TCs impact the weather patterns in downstream regions.

A key factor for the modification of the extratropical flow pattern through a transitioning TC is the reduction of potential vorticity (PV) through diabatic processes and upper-level divergent flow that impinges on the midlatitude waveguide (e.g., Riemer et al. 2008; Hodyss and Hendricks 2010; Torn 2010; Archambault et al. 2015; Torn et al. 2015). Negative PV advection by the divergent flow deflects PV contours poleward and strengthens the meridional PV gradient, which results in a downstream ridge amplification and a jet streak intensification, respectively. The ridge amplification and jet streak intensification may result in the development of a RWP that disperses eddy kinetic energy downstream (e.g., Harr and Dea 2009; Keller et al. 2014).

The upper-level divergent flow and the downstream ridge amplification can slow down the eastward propagation of an upstream trough so that the TC may phase favorably with the trough (Atallah and Bosart 2003; Riemer et al. 2008) and reach a location where the transitioning TC can impact the midlatitude flow most significantly (Riemer and Jones 2010). The phasing between the leading edge of this trough and the TC has considerable implications on the TC itself as well as on the downstream development (Ritchie and Elsberry 2007; Grams et al. 2013b). Under favorable conditions, the TC may reintensify as an extratropical low pressure system and/or excite a pronounced midlatitude Rossby wave. A shift of the TC on the order of 100 km relative to the upstream trough may result in a decay of the TC and no significant midlatitude wave amplification (Grams et al. 2013b).

At later stages of the interaction, the balanced cyclonic circulation of the decaying TC amplifies the downstream ridge through poleward advection of low PV air (Riemer et al. 2008). At the same time, the anticyclonic wind field associated with the downstream ridge and the outflow anomaly of the TC contributes to a deepening of a downstream trough. This way, an upper-level ridge–trough couplet extends downstream and cyclogenesis events may occur as part of the downstream development (e.g., Riemer et al. 2008; Archambault et al. 2013; Grams et al. 2013b).

In this study, we identify synoptic-scale RWPs as objects downstream of WNP, North Atlantic, and south Indian Ocean recurving TCs. The identification of RWPs enables us to compare their frequency and amplitude downstream of TCs to climatological values of these quantities. The identification approach and the statistical evaluation of the significance of RWP frequency and amplitude anomalies downstream of recurving TCs differ to the studies by Archambault et al. (2015) and Torn and Hakim (2015). Based on recurvature-relative composite Hovmöller diagrams of the 250-hPa meridional wind, Archambault et al. (2015) concluded that WNP TCs tend to be associated with a statistically significant amplified RWP compared to climatology that persists for approximately 10 days. By comparing RWPs downstream of TCs to RWPs downstream of extratropical cyclones, Torn and Hakim (2015) showed that RWPs associated with WNP TCs exhibit a greater peak amplitude than RWPs associated with extratropical cyclones during winter (November–March). In addition, RWPs associated with WNP TCs tend to propagate farther downstream relative to RWPs related to midlatitude cyclones in winter and fall (August–October). In contrast, RWPs downstream of North Atlantic TCs have a weaker amplitude than RWPs associated with midlatitude cyclones and do not propagate as far downstream (Torn and Hakim 2015). Hence, Torn and Hakim (2015) concluded that WNP TCs lead on average to a longer-lasting and higher-amplitude downstream response compared to extratropical cyclones, while the reverse can be observed over the North Atlantic.

Both Archambault et al. (2015) and Torn and Hakim (2015) created a subset of recurving TCs to further investigate processes that are relevant for the midlatitude flow amplification. By creating a subset based on the magnitude of negative PV advection by the irrotational wind associated with the TC, Archambault et al. (2015) showed that TCs with a strong upper-level divergent flow amplify a preexisting RWP that disperses downstream across the North Pacific to North America. The importance of a preexisting RWP for the downstream flow evolution is confirmed by Torn and Hakim (2015) who investigate subsets based on the existence or nonexistence of an upstream trough. They conclude that TCs that interact with a preexisting midlatitude trough
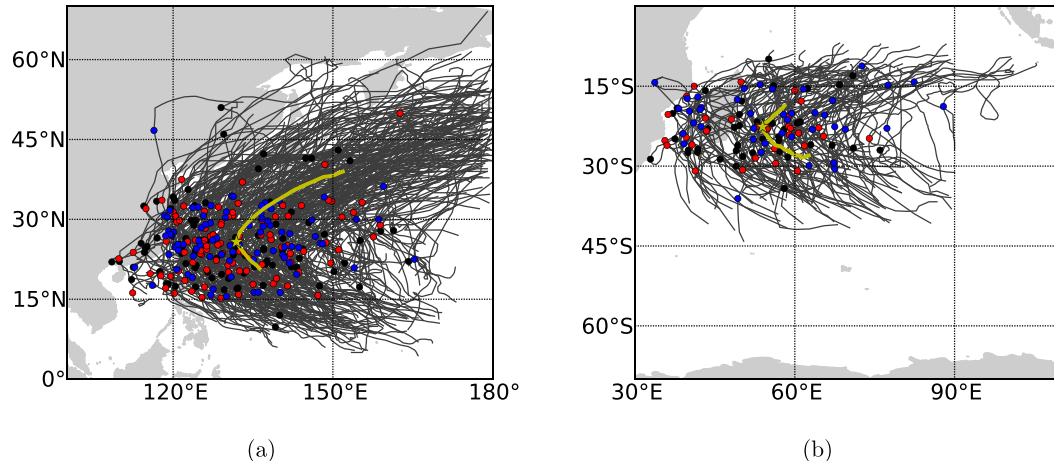
FIG. 1. Best tracks of (a) WNP TCs and (b) south Indian Ocean TCs that fulfill the criteria given in section 2a (source: International Best Track Archive for Climate Stewardship). Circles denote the position of each TC at recurvature time. Circles are colored by decade: 1980–89 (black), 1990–99 (red), and 2000–10 (blue). The yellow line gives the mean recurving track ($T − 48$ to $T + 96$ h) and the yellow star denotes the mean recurvature point.

are associated with a higher-amplitude downstream response than TCs that do not interact with an upstream trough. In this study, we present subsets for WNP TCs with and without downstream development. Despite this complementary approach we obtain quite similar results that corroborate the findings of the two previous climatological investigations.

The remainder of this paper is organized as follows. In section 2, we describe the dataset and methods we used. Section 3 presents a climatology of RWPs downstream of WNP, south Indian Ocean, and North Atlantic recurving TCs. In section 4, we investigate the synoptic conditions for WNP recurving TCs with and without a downstream Rossby wave development in a composite view using PV advection diagnostics, eddy kinetic energy analysis, and quasigeostrophic forcing diagnostics. A climatological investigation of forecast uncertainty downstream of recurving TCs in section 5 is followed by a summary and discussion of the results in section 6.

2. Dataset and methodology

a. Tropical cyclone dataset

In this study, we focus on recurving WNP and North Atlantic TCs in the period June–November 1980–2010 and on recurving south Indian Ocean TCs in the period December–April 1980–2010. The 6-hourly (0000, 0600, 1200, and 1800 UTC) TC positions are retrieved from the IBTrACS-WMO best track database (Knapp et al. 2010), which contains data from the Regional

Specialized Meteorological Centers (RSMCs). We use the time at which a TC recurved as the reference time (i.e., $T + 0$ day) for the most part of the following investigations. The TC recurvature criteria used in this study match the criteria used in a climatology of WNP TCs by Burroughs and Brand (1973). We consider only those TCs that were designated as an extratropical cyclone during their life cycle (cf. Klein et al. 2002; Jones et al. 2003; Archambault et al. 2013). In total, 280 out of 656 (42.7%) WNP TCs (Fig. 1a), 124 out of 428 (29.0%) North Atlantic TCs (not shown), and 114 out of 413 (27.6%) south Indian Ocean TCs (Fig. 1b) fulfill these criteria in the selected time period. It should be noted here that the given percentage of south Indian Ocean TCs might not represent the actual value. Griffin and Bosart (2014) identified several inconsistencies in the dataset for this ocean basin.

b. Identification of Rossby wave packets

We use the European Centre for Medium-Range Weather Forecasts (ECMWF) interim reanalysis (ERA-Interim; Dee et al. 2011) at 1° horizontal resolution to identify RWPs and to analyze the synoptic evolution from a composite perspective. A Hilbert transform filtering technique enables us to identify the RWPs. By applying the filtering technique to the meridional wind along a latitude circle, Zimin et al. (2003) extracted the envelope of synoptic-scale RWPs. This technique has the advantage that, once certain thresholds have been chosen, large datasets can be screened automatically (Glatt et al. 2011). Since we investigate meridional averages of the wave packet envelope for the most

part we adhere here to the technique described in Zimin et al. (2003) and do not use the refined method of Zimin et al. (2006).

To identify RWPs we compute the envelope of the 250-hPa meridional wind. The Hilbert transform eliminates the phase variation in longitude so that northerly and southerly winds do not cancel in a composite view. In a first step, we compute the Fourier transform of the meridional wind along a latitude circle. Second, we apply an inverse Fourier transform to a selected band $(0 < k_{min} \le k \le k_{max})$ of the positive wavenumber half of the Fourier spectrum. This enables us to restrict the zonal wavenumber range to the synoptic range $(k_{min} = 5, k_{max} = 15)$. Third, the RWP envelope along a full-latitude circle is computed by the modulus of the inverse Fourier transform. We repeat the above steps for each latitude circle in 1° steps. The concatenation of the one-dimensional envelope for each latitude circle from the equator to the pole finally yields the two-dimensional RWP envelope E over an entire hemisphere. The RWP envelope E exhibits large values in regions with a strong meridional flow component and small values in regions with a mainly zonally oriented flow.

We identify the RWPs as single objects by keeping the envelope E only in those regions where it exceeds a threshold value τ. Following Glatt and Wirth (2014) τ is defined as $\tau = \tau^* \times \overline{E}$, where τ^* is a dimensionless number and $\overline{E}$ denotes the hemispheric average of E at a given time. The usage of a threshold relative to the hemispheric average of E allows us to account for the seasonal variation of the meridional wind. In this study, we apply $\tau^* = 3.2$, which is in the range of $3 \le \tau^* \le 4$ that was suggested by Glatt and Wirth (2014). Finally, a meridional average between 20° and 80°N/S yields for each time a one-dimensional field varying in longitude only. This meridional average excludes the tropics and the poles from further consideration, but ensures that the entire extratropics are included.

c. Compositing technique and statistical evaluation

To investigate the modifications of RWP amplitude and frequency downstream of recurving TCs we apply the Hilbert transform filtering technique in 6-hourly time intervals from 7 days prior to 10 days after all TC recurvatures in the period 1980–2010. Finally, we make a Hovmöller composite temporally centered on the recurvature time. This Hovmöller composite will be referred to as a ''recurvature-relative composite'' hereafter. We choose not to composite the data on a central longitude since this would amplify the results of our recurvature-relative composite artificially in comparison to climatology and in comparison to the

randomly created composites of the Monte Carlo approach.

The mean RWP frequency $F_{i,t}$ and the mean RWP amplitude $\hat{E}_{i,t}$ defined as

$$F_{i,t} = \frac{1}{N_c} \sum_c M_{i,t}^c \quad \text{and} \quad \hat{E}_{i,t} = \frac{\sum_c E_{i,t}^c}{\sum_c M_{i,t}^c} \quad (1)$$

are investigated in the following. Here N_c denotes the number of cases, and $M_{i,t}^c$ is a mask at the data point (i, t) in the longitude–time Hovmöller diagram for case c that is set to 1 if the envelope $E_{i,t}^c > 0$. This means that the RWP amplitude is only calculated if a RWP is first identified so that it is independent of the RWP frequency.

Following Scherrer et al. (2006), we investigate the statistical significance of the results via a Monte Carlo approach. We create 1000 random Hovmöller composites of the RWP frequency and amplitude. Each of the composites consists of 280 (WNP), 114 (south Indian Ocean), and 124 (North Atlantic) cases that are centered on a randomly chosen date so that the composites contain data with and without TCs. Each date is composed of a randomly chosen year out of the period 1980–2010 and a randomly chosen day and month from a 14-day period around each recurvature that is incorporated in the recurvature-relative composite. By choosing the day from a range of days around each recurvature we account for the seasonal variability in the random composites. Finally, we determine the upper and lower 5% percentiles of the Monte Carlo composites and define those values of the recurvature-relative composite as statistically significant that either exceed or fall below these percentiles.

d. Flow decomposition

The initiation, amplification, and downstream propagation of a Rossby wave can be explained by the advection of PV anomalies through the winds induced by the circulation anomalies themselves (Hoskins et al. 1985). On isentropic levels, PV is conserved following adiabatic and frictionless motion. Thus, in regions where diabatic processes and friction are negligible the evolution of the upper-level PV can be attributed to the advection of PV along the isentropic surfaces. We quantify the contributions of the nondivergent circulation associated with the inner core of the TC, the nondivergent midlatitude flow, and the upper-level divergent flow to the Rossby wave amplification through advective processes by performing a Helmholtz partition of the flow on isentropic surfaces from 320 to 360 K at 5-K intervals. This approach follows the analysis in Riemer et al.

(2008) and Riemer and Jones (2010), but for the purposes of this study we limit the analysis to using vorticity inversion instead of PV inversion.

(i) The circulation associated with the inner core of the TC is identified as the relative vorticity within a fixed radius around the TC center, which is defined as the minimum in mean sea level pressure. A successive overrelaxation method enables us to compute the rotational wind $\mathbf{v}_{\psi\mathrm{TC}}$ induced by the relative vorticity ζ_{TC}. We tested the results for various radii around the TC center and chose a radius of 600 km for which an adequate distinction between the cyclonic inner core circulation and the surrounding flow features (e.g., the anticyclonic TC outflow anomaly) was possible.

(ii) The upper-level divergent wind $\mathbf{v}_{\chi}$ is computed from the full divergence via successive overrelaxation. The upper-level divergent flow cannot be attributed straightforwardly to a specific flow feature since the upper-level divergence related to the TC inner core convection or the outflow associated with slantwise ascent along a baroclinic zone do not appear as spatially distinct features. Hence, we avoid the term ''outflow associated with the TC'' since it is inappropriate to talk about the outflow of one specific system.

(iii) The nondivergent midlatitude wind $\mathbf{v}_{\psi\mathrm{midlat}}$ is computed as the difference between the total wind $\mathbf{v}$, $\mathbf{v}_{\psi\mathrm{TC}}$, and $\mathbf{v}_{\chi}$ (i.e., $\mathbf{v}_{\psi\mathrm{midlat}} = \mathbf{v} - \mathbf{v}_{\psi\mathrm{TC}} - \mathbf{v}_{\chi}$). It should be noted that $\mathbf{v}_{\psi\mathrm{midlat}}$ comprises the winds associated with the large-scale anticyclone, the developing midlatitude Rossby wave, the anticyclonic outflow anomaly of the TC, as well as the flow induced by the interaction between the ET system and the midlatitude flow. A further separation would require a piecewise PV inversion, which would go beyond the scope of this study.

e. Quasigeostrophic forcing diagnostic

To assess the contribution of dry dynamics to vertical motion during the TC–midlatitude flow interaction, we compute a height attributable solution of the quasigeostrophic (QG) omega equation in **Q**-vector form (Clough et al. 1996; Hoskins et al. 1978). This diagnostic allows us to estimate the importance of adiabatic forcing for vertical motion compared to diabatically driven vertical motion associated with the TC and with its interaction with the midlatitude baroclinic zone, as the QG diagnostic strongly underestimates vertical motion in regions with intense latent heating (Boettcher and Wernli 2011). In addition, the diagnostic enables us to investigate the contribution of different vertical levels to

the QG vertical motion between 1000 and 100 hPa. In this study, the contribution of the lower troposphere (1000–750 hPa) is distinguished from the contribution of weather systems in the upper troposphere (500–100 hPa) similar to studies by Deveson et al. (2002) and Dacre and Gray (2009).

f. Eddy kinetic energy diagnostic

Alternative to the PV perspective, the amplification and downstream propagation of a Rossby wave can be explained in an eddy kinetic energy (K_e) framework. The diagnostic allows us to identify sources of K_e that contribute to the amplification of the midlatitude flow. In addition, the combination of the K_e diagnostic and the QG diagnostic (section 2e) helps to quantify the importance of adiabatic forcing of vertical motion for the local generation of K_e. The K_e framework has been successfully applied to describe characteristics of downstream development associated with TC–midlatitude flow interactions (Harr and Dea 2009; Keller et al. 2014). These studies showed that TCs may act as an additional K_e source, supporting the amplification of midlatitude wave packets.

Following Orlanski and Sheldon (1995), the energy budget is computed as the sum of a time mean (subscript m) and a perturbation. The horizontal wind field is then defined as $\mathbf{V} = \mathbf{V}_m + \mathbf{v}$ and scalar variables, including the vertical velocity ω, are defined as $Q = Q_m + q$. The time mean is defined as a 30-day running mean. The time tendency of $K_e = 1/2|\mathbf{v}|^2$ is defined in pressure coordinates as

$$\frac{\partial K_e}{\partial t} = -\nabla_p \cdot (\mathbf{v}\phi)_a - \omega\alpha - \frac{\partial(\omega\phi)}{\partial p} - \nabla_p \cdot (\mathbf{V}K_e)$$
$$- \frac{\partial(\omega K_e)}{\partial p} - \mathbf{v} \cdot (\mathbf{v} \cdot \nabla_p \mathbf{V}_m) + \text{residue}, \quad (2)$$

where ϕ denotes the geopotential height, α the specific volume, and ∇_p the horizontal gradient operator. The first term on the right-hand side is the ageostrophic (subscript a) geopotential flux divergence. This term describes the dispersion of energy between adjacent K_e maxima that are typically located on the flanks of midlatitude troughs and ridges. The ageostrophic flux divergence steers the entire RWP with group velocity. The second term represents the baroclinic conversion from available eddy potential energy to K_e. The fourth term is the horizontal K_e flux divergence, describing the propagation of K_e maxima with phase velocity. The sixth term defines the barotropic conversion between the eddies and the mean flow. In this study, the K_e tendency terms are vertically integrated between 1000 to 100 hPa to consider the K_e distribution in the entire troposphere.
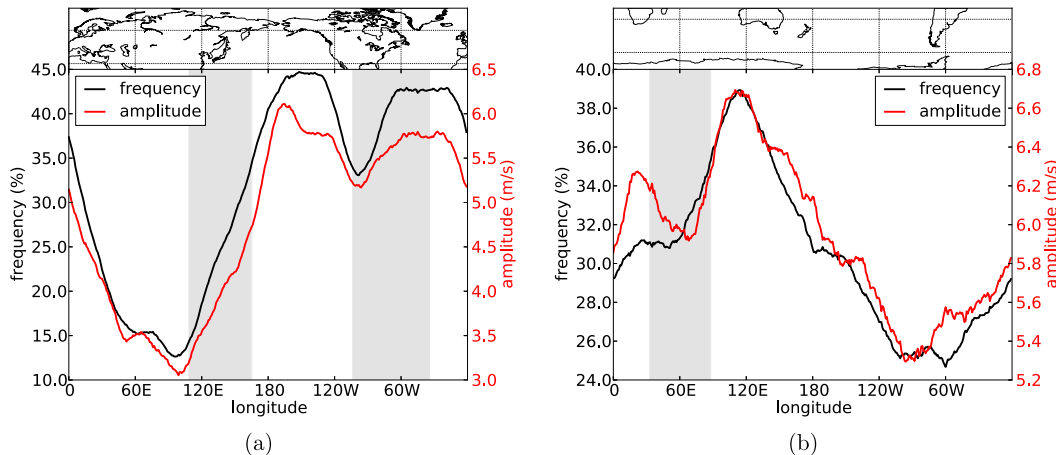
FIG. 2. Mean RWP frequency (%) and mean RWP amplitude (m s^{-1}) (a) over the Northern Hemisphere and (b) over the Southern Hemisphere during June–November and December–April, respectively. Note the different scale for the *y* axes in (a),(b). The gray shading indicates the range of longitudes of recurving TCs that are included in this study.

This vertical integration allows us to neglect the third and fifth term of Eq. (2). The normalization of the vertically integrated terms with the gravitational acceleration yields the equation for temporal changes of K_e:

$$\frac{1}{g}\int_{1000}^{100}\frac{\partial K_e}{\partial t}\,dp = \frac{1}{g}\int_{1000}^{100}\left[-\nabla_p\cdot(\mathbf{v}\phi)_a - \omega\alpha - \nabla_p\cdot(\mathbf{V}K_e) - \mathbf{v}\cdot(\mathbf{v}\cdot\nabla_p\mathbf{V}_m) + \text{residue}\right]dp. \tag{3}$$

3. Rossby wave packets downstream of recurving TCs

a. Climatology of Rossby wave packets

To determine deviations of RWP frequency and amplitude in the recurvature-relative composite from climatology we compute a climatology of both quantities. Thereby, we focus on the months June–November for the Northern Hemisphere and December–April for the Southern Hemisphere. In the Northern Hemisphere, the lowest values of RWP frequency and amplitude occur over the Eurasian continent between 50° and 120°E (Fig. 2a). The climatological frequency exhibits minimum values of about 13% with a minimum amplitude of about 3 m s^{-1}. Highest RWP frequencies of 40%–45% can be found in the storm-track regions over the eastern North Pacific and the western North Atlantic.

The zonal variability of the climatological RWP frequency and amplitude in the Southern Hemisphere is much lower than in the Northern Hemisphere (Fig. 2b). The highest RWP frequency of more than 35% can be found over the eastern south Indian Ocean and Australia between 90° and 150°E. The lowest values of about 25% occur over South America. The amplitude varies between the maximum values of 6.7 m s^{-1} over the

eastern south Indian Ocean and the lowest values of 5.3 m s^{-1} over South America. A climatological investigation by Souders et al. (2014) showed a similar spatial distribution of RWP frequency for both hemispheres for the period 1979–2010.

b. RWPs downstream of western North Pacific TCs

The RWP frequency downstream of recurving TCs exceeds the climatological value from the WNP to central North America (Fig. 3a). A statistically significant RWP frequency anomaly of 6%–9% occurs over the WNP already one day after recurvature. This positive RWP frequency anomaly over the WNP suggests that recurving TCs lead to a westward extension of Rossby wave activity relative to climatology. The eastward extension of the statistically significant RWP frequency anomaly with time indicates downstream Rossby wave dispersion in the recurvature-relative composite. Maximum RWP frequency anomalies of more than 12% occur along 180° 2–3 days after recurvature; 3–5 days after recurvature, a relative minimum occurs in the RWP frequency anomaly over the eastern North Pacific. This relative minimum can be potentially attributed to the climatological RWP frequency that reaches maximum values in this region
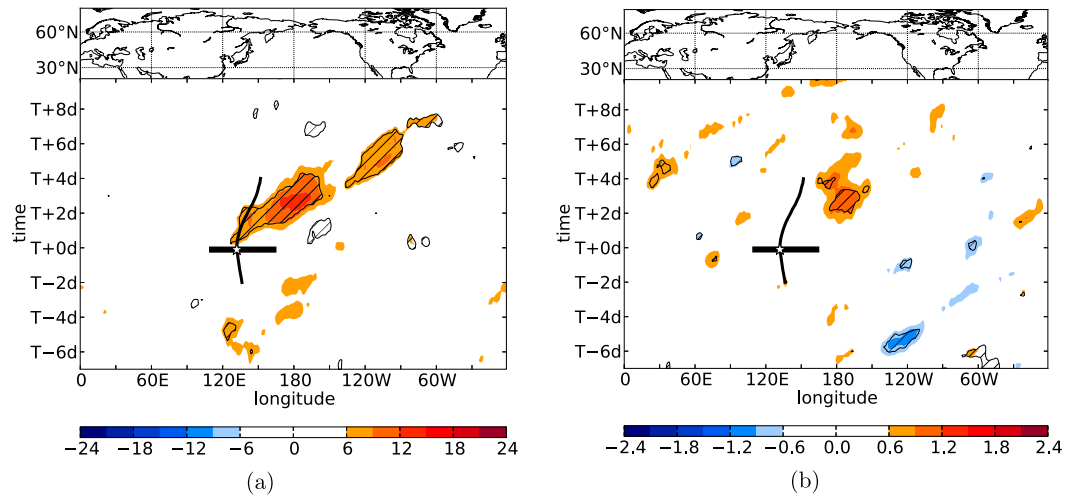
FIG. 3. Recurvature-relative composites of (a) RWP frequency anomaly (shaded in %) and (b) RWP amplitude anomaly (shaded in $m s^{-1}$) relative to June–November climatology for WNP TCs. Values that are statistically significant at the 95% confidence level are hatched. Black thick line gives the mean recurving track ($T - 48$ to $T + 96$ h) and the white star denotes the mean recurvature point. Black horizontal bar marks the range of longitudes of the TCs at recurvature. Data are smoothed with a Gaussian filter.

(Fig. 2a). In addition, the occurrence of the breaking of high-amplitude waves might also contribute to the local reduction of RWP frequency. A second positive RWP frequency anomaly of more than 6% exists 4–7 days after recurvature over western North America. The statistical significance and the anomaly of RWP frequency decrease rapidly about one week after the time of recurvature over central North America. The RWP amplitude is amplified significantly over the central Pacific 2–4 days after recurvature (Fig. 3b).

A major advantage of choosing recurvature time as reference time, rather than the time when a former TC was classified for the first time as an extratropical cyclone, is the fact that recurvature time can be determined objectively from the best track data. However, the temporal lag between recurvature time and the time of the TC–midlatitude flow interaction may exhibit a strong case-to-case variability. To test the sensitivity of our results to the choice of the reference time, we compute the anomalies of RWP frequency and amplitude for the same TCs, but centered on the time when the RSMC classified the former TC for the first time as an extratropical cyclone (EC). This framework will be referred to as an "EC-relative composite" hereafter. In the EC-relative composite the anomalies of RWP frequency and amplitude are stronger than in the recurvature-relative composite. The frequency anomaly reaches values of more than 15% over the western to central North Pacific (Fig. 4a). Also, the anomalies over western to central North America are slightly stronger than the anomalies in the recurvature-relative composite. The RWP amplitude exceeds the climatological

value by up to $1.8 m s^{-1}$ between 180° and 150°W (Fig. 4b), which corresponds to a relative increase of 30% compared to climatology (not shown). This positive anomaly over the central North Pacific seems to be a robust feature as it occurs in the recurvature-relative composite as well as in the EC-relative composite. A positive RWP amplitude anomaly over western North America is sensitive to the reference time as it does not occur in the recurvature-relative composite. The statistically significant increase of RWP amplitude reveals that RWPs that are associated with TCs are stronger than those that generally occur in midlatitudes.

The initial increase of the RWP amplitude (Fig. 4b) occurs about 1–2 days later than the increase of RWP frequency (Fig. 4a). This indicates that the TCs interact with upstream midlatitude disturbances, which are part of initially rather weak RWPs. During the interaction with the TCs the RWPs amplify so that downstream disturbances that are still part of the same initial RWP exhibit a much higher amplitude.

The RWP frequency is significantly enhanced over western and central North America in the recurvature-relative composite as well as in the EC-relative composite. Instead, the RWP amplitude is only enhanced over western North America. Hence, Rossby waves are more likely over central North America after recurving WNP TCs, but their amplitude is not necessarily enhanced compared to climatology.

The discrepancies between the recurvature-relative composite and the EC-relative composite can be potentially attributed to the variance of the temporal lag between the reference times and the time of the
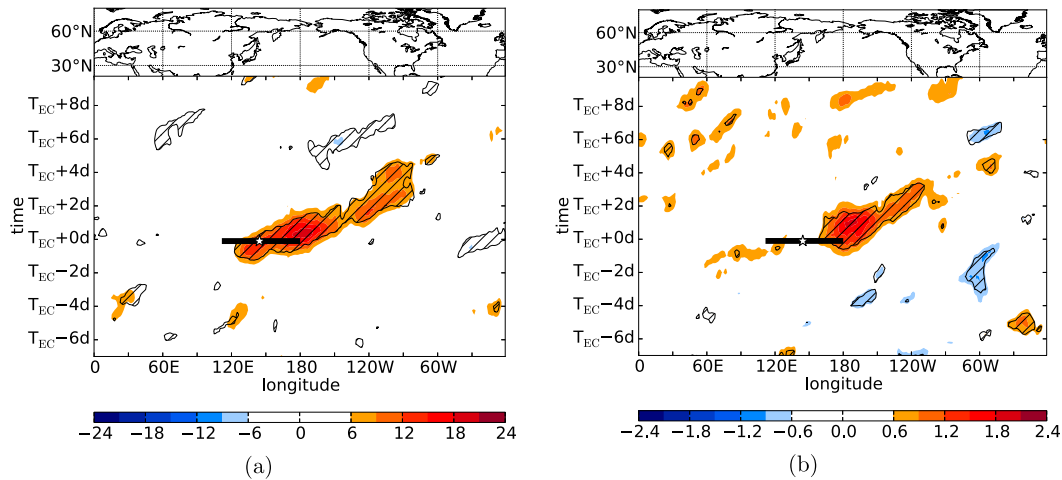
FIG. 4. As in Fig. 3, but relative to the time $T_{EC} + 0$ day when the TCs were first classified as an extratropical cyclone by the RSMC. Black horizontal bar marks the range of longitudes of the TCs at T_{EC}. White star marks the mean longitude of all TCs at T_{EC}.

TC–midlatitude flow interaction. A comparison of the temporal lag between the reference times used in this study and the time of maximum TC–midlatitude flow interaction, defined by the magnitude of negative PV advection by the irrotational wind associated with the TC (Archambault et al. 2013), reveals that the variability of the temporal lag between recurvature time and the maximum interaction time is greater than between the time when the TC was defined as EC and the maximum interaction time (not shown). The sensitivity of composites to the choice of the reference time was also noted by Torn and Hakim (2015). Meridional wind anomalies downstream of WNP TCs were weaker in recurvature-relative composites than in composites centered on the time of ET onset (Hart 2003). A future study could investigate the change of RWP frequency and amplitude in a composite relative to the time of the maximum TC–midlatitude flow interaction (Archambault et al. 2013, 2015) or to the time of ET onset (Hart 2003; Torn and Hakim 2015).

c. RWPs downstream of North Atlantic TCs

Case studies have highlighted the impact of North Atlantic TCs on the downstream midlatitude flow that can lead to high-impact weather in downstream regions (e.g., Agusti-Panareda et al. 2004; Grams et al. 2011; Pantillon et al. 2015). However, we do not observe a statistically significant increase in RWP frequency and amplitude downstream of in total 129 recurving TCs in this basin (not shown). The results of the case studies and of this study indicate that North Atlantic TCs are able to modify RWPs, but that these RWPs do not depart significantly from RWPs that generally occur in

midlatitudes. A possible explanation is that the climatological RWP frequency and amplitude are higher in this region than over the WNP (Fig. 2a). The climatological RWP frequency exhibits values of 15%–40% over the WNP, whereas it reaches values from 33% to 43% over the North Atlantic. Therefore, a westward extension of the Rossby wave activity as observed for the WNP-recurving TCs does not occur. In addition, as pointed out by Riemer and Jones (2014), TC–midlatitude flow interactions can initiate the breaking and decay of high-amplitude Rossby waves. In particular, the climatologically short and weak waveguide over the North Atlantic compared to the WNP may favor the conditions for anticyclonic Rossby wave breaking and may limit the downstream flow response (Archambault et al. 2015).

d. RWPs downstream of south Indian Ocean TCs

The RWP frequency is significantly amplified by 12%–15% downstream of recurving south Indian Ocean TCs (Fig. 5a). The RWP frequency starts to increase significantly 2 days after recurvature in downstream regions. A relative minimum of RWP frequency over Australia is followed by a further significant RWP frequency anomaly of 12%–15% over the western South Pacific 5–7 days after recurvature time. Thus, once a RWP has been amplified by the recurving TC it has the ability to propagate from the western south Indian Ocean to the western South Pacific.

The RWP amplitude anomaly is considerably stronger than downstream of WNP TCs. We observe a statistically significant amplification of the RWP amplitude by more than $1.8 \, \mathrm{m \, s^{-1}}$ between 100° and 160°E from 3 to
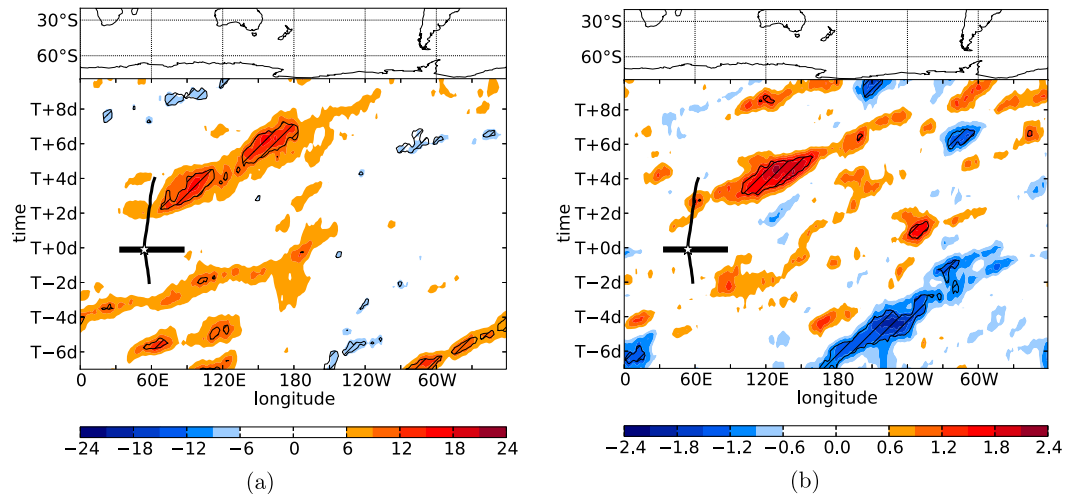
FIG. 5. As in Fig. 3, but for anomaly relative to December–April climatology for the western south Indian Ocean TCs.

5 days after recurvature time (Fig. 5b). This anomaly corresponds to a relative increase of RWP amplitude by about 30% (not shown). Interestingly, the RWP amplitude anomaly is strongest over Australia where the RWP frequency is not significantly anomalous. Thus, TC-related RWPs over Australia exhibit a much stronger amplitude than climatology, but are not necessarily more frequent than climatology.

A remarkable feature of the composite is a negative RWP amplitude anomaly over the South Pacific 7–2 days prior to recurvature. This negative anomaly indicates a rather zonal flow far upstream of the TCs. A thorough analysis of this negative anomaly and its linkage to the positive RWP anomaly downstream of the south Indian Ocean TCs goes beyond the scope of this study.

The anomalies are less coherent in a framework relative to the time when the TC was classified as an EC by the RSMC (not shown). This can be potentially attributed to the inconsistencies concerning the classification of ECs in the south Indian Ocean best track dataset by the RSMC as documented by Griffin and Bosart (2014).

4. Composite analysis of cases with and without Rossby wave development

a. Identification of cases

The identification of RWPs as separate objects enables us to select cases with and without Rossby wave development downstream of the WNP recurving TCs. By doing so, we are able to make a classification based on the downstream flow response that is independent of the structure of the TC. However, this does not imply

that the TCs in the cases without downstream Rossby wave development do not have an impact on the midlatitude flow. For example, TCs that interact with the midlatitude flow may lead to a jet intensification that is not necessarily followed by a downstream Rossby wave development (Grams et al. 2013a). This type of classification based on the downstream flow response is complementary to the studies by Archambault et al. (2013, 2015) who distinguished between two scenarios based on a TC–midlatitude flow interaction metric independent of the downstream flow response.

We define a mask by the 95% confidence level of the Monte Carlo approach between $-10°$ and $80°$ relative to the longitude of recurvature of each TC and from recurvature time to 5 days after recurvature (Fig. 6). Then, we determine for each case the percentage of grid points in this mask that have a Rossby wave amplitude greater than zero. The quintile of cases that exhibit the highest percentage is in the following defined as Rossby wave case (RW case). The quintile of cases that exhibit the lowest percentage is defined as no Rossby wave case (no-RW case). Each quintile comprises 56 recurving TCs.

The RWP frequency anomaly varies between 30% to more than 40% in the RW case composite in the range of the mask (Fig. 6a). The climatological RWP frequency exhibits values between 20% and 45% in that region (Fig. 2a). The absolute values of RWP frequency for the RW case composite vary between 60% to more than 90% (not shown). Interestingly, the positive anomaly of more than 10% extends from the WNP to the North Atlantic. Hence, the RW case composite potentially contains cases in which a Rossby wave reached the North Atlantic 10 days after the
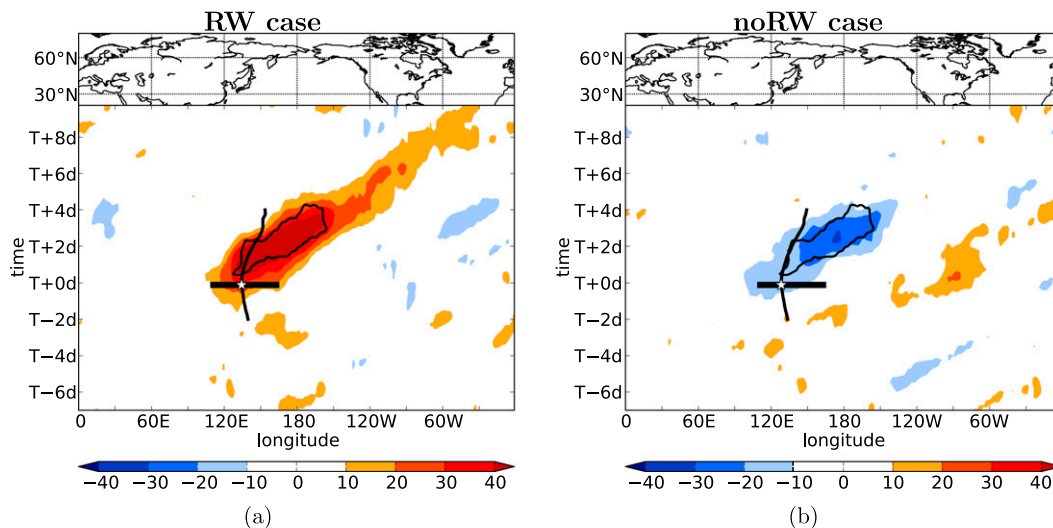
FIG. 6. Anomaly of RWP frequency (shaded in %) relative to June–November climatology for (a) RW case and (b) no-RW case for the WNP TCs. The black contour indicates the mask that we used to determine the lower and upper quintile (56 events). The black thick line gives the mean recurving track ($T - 48$ to $T + 96$ h) for each case and the white star denotes the mean recurvature point. Black horizontal bar marks the range of longitudes of the TCs at recurvature. Data are smoothed with a Gaussian filter.

recurvature of a WNP TC. The composite for the no-RW case exhibits RWP frequency anomalies between -10% and -30% in the range of the mask (Fig. 6b). With a climatological RWP frequency of 20%–45%, the absolute values of RWP frequency vary between 0% and 30% in the no-RW case composite in the range of the mask (not shown).

To analyze the propagation of the Rossby wave in the RW case as well as in the no-RW case, we create composites of the meridional wind at 250 hPa. To obtain clear composite fields, these composites are centered on the central longitude at recurvature time. A precursor Rossby wave emanates from the Asian continent in the RW case (Fig. 7a). A weak ridge exists at 90°E already
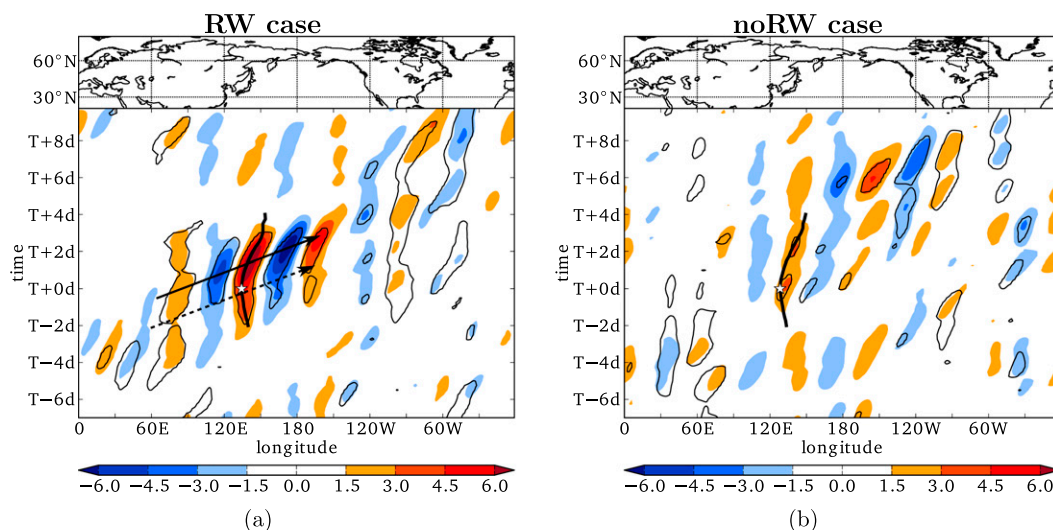

FIG. 7. (a) RW case and (b) no-RW case recurvature-relative composite Hovmöller diagrams of the 20°–80°N-averaged 250-hPa meridional wind (shaded in m s^{-1}) for zonal wavenumbers 5–15. Black contours denote the statistical significance at the 99% confidence level based on a two-sided Student's t test. The black thick line gives the mean recurving track ($T - 48$ to $T + 96$ h) for each case and the white star denotes the mean recurvature point. The dashed and solid black arrows in (a) indicate the estimated zonal group velocity of the Rossby wave based on the leading edge and the peak amplitude, respectively.

4 days prior to recurvature and a trough develops downstream with its axis being located about 15°W of the approaching TC. The TC itself is located in a southerly flow associated with the eastern flank of this upstream trough. This southerly flow amplifies strongly immediately after the recurvature. This amplification indicates an interaction between the transitioning TC and the midlatitude flow. The alignment of the maximum in southerly winds with the TC track reveal that the TC propagates eastward with the phase velocity of the upstream trough. A statistically significant RWP pattern develops downstream before the signal decreases about 3 days after recurvature time over the eastern North Pacific. The estimated group velocity of the RWP is about 40° day^{-1}, which is comparable to the group velocity of the RWP downstream of all WNP recurving TCs identified in Archambault et al. (2015).

In the no-RW case, a precursor wave packet can be hardly identified (Fig. 7b). A weak ridge starts to develop in situ between 120°E and 180° around recurvature time. This suggests that the transforming TC interacts with the midlatitude flow and contributes to a weak amplification of the meridional wind. Interestingly, a second Rossby wave pattern starts to develop 5 days after recurvature time. This rather weak, but statistically significant RWP propagates downstream and reaches western North America about one week after recurvature time.

The results suggest that a precursor Rossby wave emanating from the Asian continent provides favorable conditions for a Rossby wave development downstream of WNP recurving TCs. However, the existence of a precursor Rossby wave does not necessarily result in a strong downstream development. The development of the transitioning TC and the downstream flow amplification strongly depend on the phasing between the transitioning TC and the midlatitude flow (Klein et al. 2002; Ritchie and Elsberry 2007; Grams et al. 2013b). The systematic investigation of the phasing between the midlatitude flow and the TCs in the RW and no-RW case could be a task for future studies.

b. Characteristics of the TCs at recurvature

Tropical cyclones associated with a downstream Rossby wave development occur more frequently in August–September and less frequently in June, July, October, and November relative to the climatological distribution of recurving TCs (Fig. 8). Recurving TCs that are not followed by a downstream Rossby wave development occur more frequently in June and September–November and less frequently in July and August relative to the climatological distribution of recurving TCs. A statistically significant difference according to a two-sided Student's *t* test between the mean
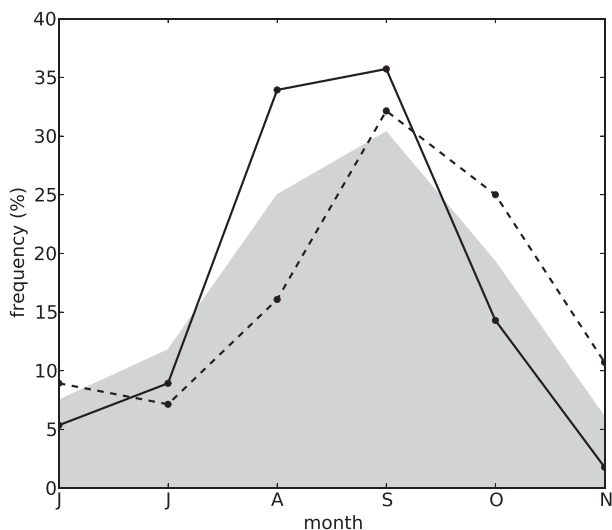

FIG. 8. Monthly frequency distribution of all recurving WNP TCs (gray fill), and of RW case TCs (solid curve) and no-RW case TCs (dashed curve).

recurvature date of the RW and no-RW case TCs could not be identified. Interestingly, the RW case TCs occur less frequently in October and November than the no-RW case TCs. This finding stands in contrast to the findings of Archambault et al. (2013). They found that strong interacting TCs, which are on average associated with stronger downstream flow response occurred in October and November more frequently than weak interacting TCs. We hypothesize that this apparent discrepancy is related to the structural changes of the jet between summer and fall. A stronger jet and hence a stronger PV gradient in November result in enhanced values of PV advection by the upper-level divergent wind when a TC interacts with the midlatitude flow. Thus, assuming that the upper-level divergent flow during TC–midlatitude flow interaction is similar for summer and fall events, the number of strong interaction cases peaks late in the TC season. However, the strong interaction cases in November are not necessarily associated with downstream development. An intense jet in November might inhibit the development of a strong meridional flow (Riemer et al. 2008) so that the RW case TCs occur less frequently during this month.

To determine a potential sensitivity of the Rossby wave response to characteristics of the TCs (size, central pressure), we investigate various properties of the RW and no-RW case TCs. According to the best track data, RW case TCs are on average somewhat larger and more intense than the no-RW case TCs. The mean sea level pressure of the RW case TCs is 963 hPa at recurvature time (Fig. 9a). The no-RW case TCs exhibit a mean sea level pressure of 967 hPa. The distributions of the
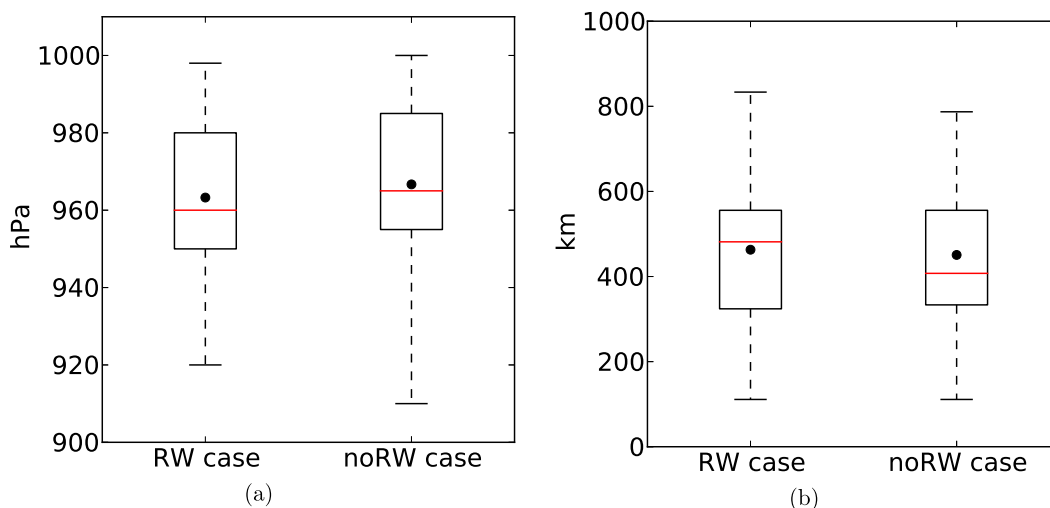
FIG. 9. Box plots showing (a) mean sea level pressure (hPa) and (b) length of the maximum $15.4\,\mathrm{m\,s^{-1}}$ wind radius (km) for the RW case TCs and no-RW case TCs at recurvature time. The length of the maximum $15.4\,\mathrm{m\,s^{-1}}$ (30 kt) wind radius was derived from the Japan Meteorological Agency best track dataset. The lower and upper bounds of each box give the 25th and 75th percentiles, respectively; the red bar and the black circle inside each box denote the median and mean, respectively; and the whiskers extend from the 25th and 75th percentiles to the 5th and 95th percentiles, respectively.

maximum $15.4\,\mathrm{m\,s^{-1}}$ (30 kt) wind radius are very similar for the RW case TCs and the no-RW case TCs (Fig. 9b). The mean length of the maximum $15.4\,\mathrm{m\,s^{-1}}$ wind radius of the RW (no-RW) case TCs is about 460 (450) km. The differences in mean sea level pressure and in the mean length of the $15.4\,\mathrm{m\,s^{-1}}$ wind radius are not statistically significant. This agrees well with findings of Archambault et al. (2013). They concluded that the amplification of the North Pacific meridional flow pattern is relatively insensitive to TC intensity and size at recurvature time.

c. Dynamics of RW and no-RW cases at recurvature

We create composite maps of PV advection (section 2d) and K_e budgets (section 2f) to contrast the synoptic development in the no-RW and RW case. The composites are computed from ERA-Interim reanalyses at 1° horizontal resolution. To account for the poleward convergence of the meridians we interpolate the data for each case onto a Cartesian grid, center the grid on the mean position of the 56 TCs in each scenario (according to the best track data), and interpolate the data back on a regular latitude–longitude grid. The PV advection diagnostic (section 2d) is computed on isentropic surfaces from 320 to 360 K at 5-K intervals for the no-RW and RW case TCs. The choice of vertical levels accounts for the seasonal variability of tropopause height and ensures that the upper-level divergent flow associated with the ET of strong TCs is incorporated in the composites. In the following, we discuss the composite fields

of PV advection and the vertically integrated K_e budget terms at recurvature time and 2 days after recurvature. (The interested reader is referred to supplemental Fig. S1 in the online supplemental material to get an overview of the full evolution from one day prior to recurvature to three days after recurvature.)

The northward deflection of the waveguide downstream of the TC indicates a ridge in both cases at recurvature time (Fig. 10). However, a pronounced trough exists only upstream of the RW case TC. In both cases, the TCs are located about 15°S of the midlatitude waveguide. The TC inner core relative vorticity is still clearly distinguishable from the midlatitude flow (see supplemental Fig. S2 in the online supplemental material) and does not induce PV advection along the midlatitude waveguide (Figs. 10a,d). This suggests that the cyclonic circulation associated with the inner core of the TC does not contribute significantly to the midlatitude flow evolution at recurvature time.

A significant contribution to the midlatitude flow modification comes from the PV advection through the upper-level divergent flow. At recurvature time, the lower- to midtropospheric ascent (Fig. 11) is associated with the TC inner core and the interaction between the TC and the still relatively weak midlatitude baroclinic zone (see supplemental Fig. S3 in the online supplemental material for full evolution). The resulting divergent winds to the north and northeast of the TC center impinge on the upper-level PV gradient (Figs. 10b and 10e). The ascent in the interaction region
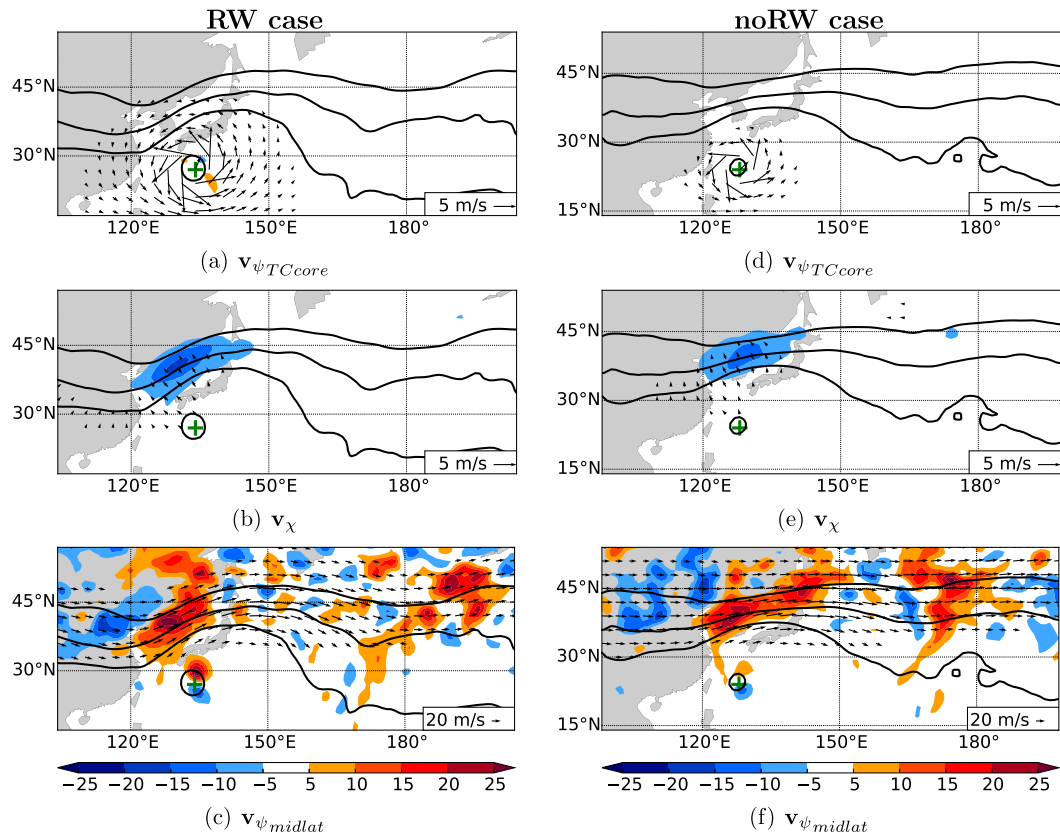
FIG. 10. (a)–(c) RW case and (d)–(f) no-RW case TC-relative composite analyses of 320–360-K PV (contoured in black at 1, 2, and 4 PVU) (1 PVU = 10^{-6} K kg^{-1} m^2 s^{-1}) and 320–360-K PV advection (shaded in 10^{-6} PVU s^{-1}) induced by the 320–360-K winds given at bottom right (vectors in m s^{-1}) at recurvature time. For illustrative purposes the coastlines are shown relative to the mean TC position (green cross).

is stronger for the RW case leading to enhanced divergent outflow from the baroclinic region and thus enhanced PV advection on the western flank of the downstream ridge. The elongated ascent region extending

along the low-level baroclinic zone (Fig. 11) and the upper-level divergent flow to the northeast of the ascent region (Figs. 10b,e) are indicative of the divergent outflow being predominantly associated with ascent up
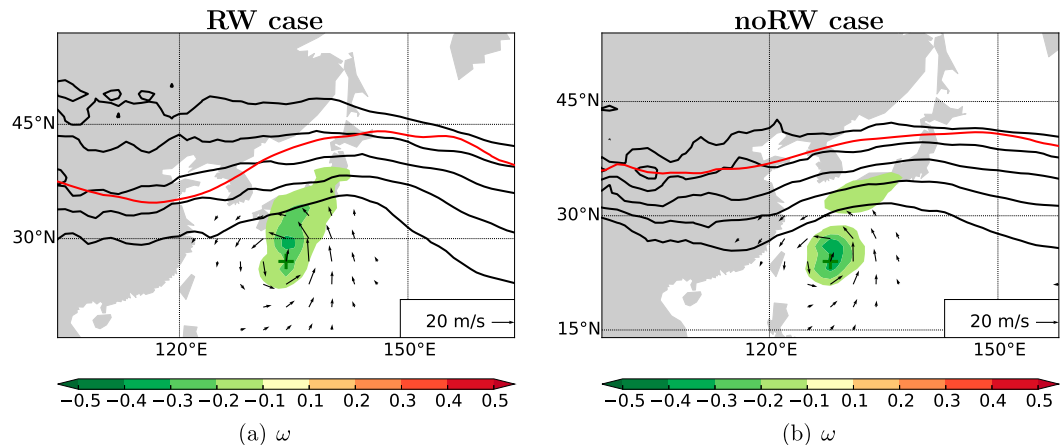

FIG. 11. (a) RW case and (b) no-RW case TC-relative composite analyses of 700–500-hPa vertical velocity (shading in Pa s^{-1}), 900-hPa winds (vectors in m s^{-1}), 900-hPa temperature (black contours from 284 to 292 K with 2-K contour interval), and 320–360-K PV (contoured in red at 2 PVU) at recurvature time. For illustrative purposes the coastlines are shown relative to the mean TC position (green cross).
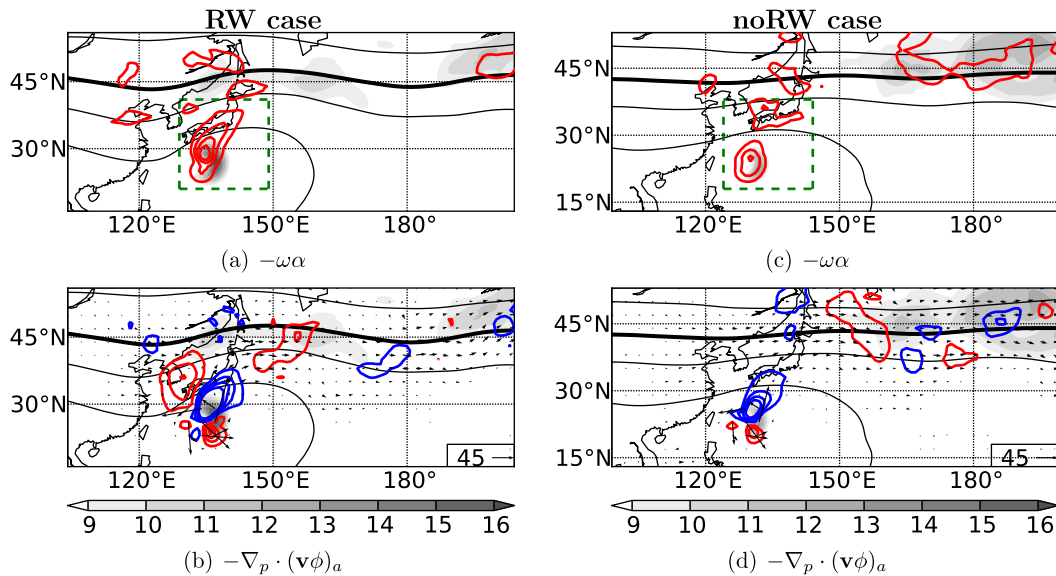
FIG. 12. (a),(b) RW case and (c),(d) no-RW case TC-relative composite analyses of vertically integrated K_e (shaded in $10^5 \, \mathrm{J \, m^{-2}}$), 200 hPa geopotential (contoured in black at $200 \, \mathrm{m^2 \, s^{-2}}$ intervals, thick black line illustrates $11\,800 \, \mathrm{m^2 \, s^{-2}}$ isoline), and vertically integrated K_e budget terms given in subcaptions (colored contours at $8 \, \mathrm{W \, m^{-2}}$ intervals) at recurvature time. (b),(d) Ageostrophic geopotential flux vectors (reference vector in $10^6 \, \mathrm{W \, m^{-1}}$). The green box in (a),(c) shows the region over which the mean baroclinic conversion was computed. For illustrative purposes the coastlines are shown relative to the mean TC position.

the sloping baroclinic zone. This ascent is being fed by moist air moving around the low-level TC core. The low-level inflow into the ascent region is stronger for the RW case, allowing a stronger diabatic enhancement of the ascent, the upper-level outflow from the baroclinic zone, and the negative PV advection to occur in the RW case.

Composites of baroclinic conversion confirm the importance of the interaction between the TC and the baroclinic zone (Figs. 12a and 12c). In the RW case as well as in the no-RW case composites, baroclinic conversion to the north of the TC reveals lifting of warm air masses and the generation of K_e. The total baroclinic conversion is higher for the RW case as it extends into the interaction region. Divergence of the ageostrophic geopotential flux superposes the region of baroclinic conversion (Figs. 12b,d). This flux divergence and the ageostrophic fluxes themselves reveal that the locally generated K_e is at least partly dispersed toward the midlatitude flow.

To quantify the importance of dry dynamics for the local generation of K_e along the baroclinic zone, we compute the baroclinic conversion term in Eq. (3) from the QG vertical motion (section 2e). Finally, we average the baroclinic conversion in a box of $20° \times 20°$ as shown in Figs. 12a,c. At recurvature time, neither the baroclinic conversion through QG ascent nor the baroclinic conversion computed from the model vertical wind field

differ significantly between the RW and no-RW case (Table 1). The baroclinic conversion computed from the model vertical motion is much stronger than the baroclinic conversion computed from the QG ascent (Fig. 13). The QG ascent accounts for 22% (15%) of the total baroclinic conversion in the RW (no-RW) case composite (Table 1). The upper-level forced QG ascent dominates at this time with 18% and 12%, respectively (see also supplemental Fig. S4 in the online supplemental material). Thus, lower-tropospheric warm air advection to the east of the TC does likely not contribute to ascent along the baroclinic zone at recurvature time.

TABLE 1. Ratio between baroclinic conversion through low-level forced QG ascent ($-\omega_{\mathrm{QG}_l}\alpha$), upper-level forced QG ascent ($-\omega_{\mathrm{QG}_u}\alpha$), the full QG ascent ($-\omega_{\mathrm{QG}}\alpha$), and the model vertical wind field ($-\omega\alpha$) for the RW and no-RW case at recurvature time. The bottom two rows give the absolute values of baroclinic conversion through QG vertical motion and the model vertical wind field, and the confidence levels for the significance of the differences between the RW and no-RW case based on a Mann–Whitney U test. The box over which the baroclinic conversion was averaged is shown in Fig. 12.

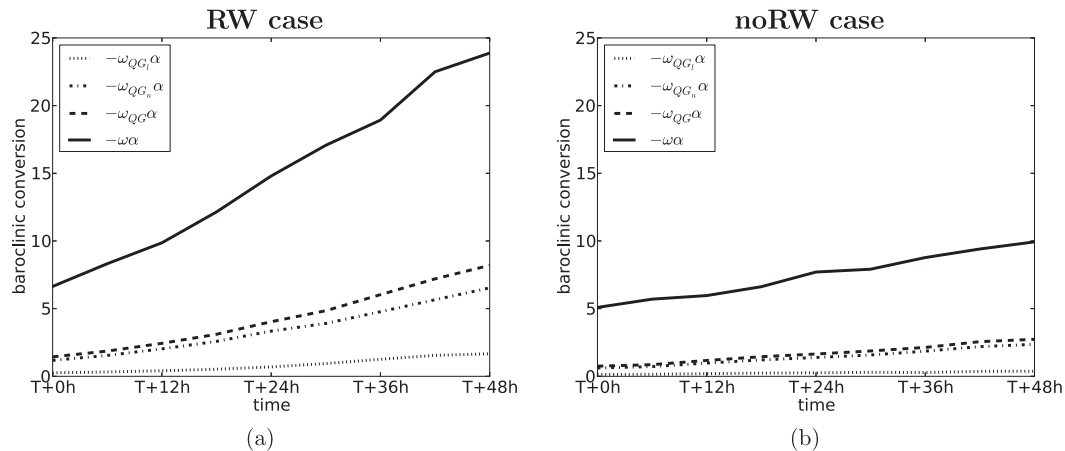|	Confidence level	RW case	No-RW case
$\omega_{\mathrm{QG}_l}\alpha/\omega\alpha$ (%)		4	3
$\omega_{\mathrm{QG}_u}\alpha/\omega\alpha$ (%)		18	12
$\omega_{\mathrm{QG}}\alpha/\omega\alpha$ (%)		22	15
$\omega_{\mathrm{QG}}\alpha$ ($\mathrm{W \, m^{-2}}$)	77.1%	1.4	0.7
$\omega\alpha$ ($\mathrm{W \, m^{-2}}$)	55.8%	6.6	5.1

FIG. 13. (a) RW case and (b) no-RW case average baroclinic conversion through low-level forced QG ascent ($-\omega_{QG_l}\alpha$), upper-level forced QG ascent ($-\omega_{QG_u}\alpha$), the full QG ascent ($-\omega_{QG}\alpha$), and the model vertical wind field ($-\omega\alpha$) in W m^{-2} between recurvature time and 2 days after recurvature. The box over which the average was performed is shown in Figs. 12 and 16.

The relatively small contribution of QG ascent to the total baroclinic conversion suggests that K_e is predominantly generated through ascent associated with diabatic processes.[1]

The magnitude of the negative PV advection through the upper-level divergent wind associated with this region of vertical motion is slightly stronger in the RW case than in the no-RW case (Figs. 10b and 10e). In addition, the location of strongest negative PV advection relative to the downstream ridge varies between the cases. For the no-RW case, negative PV advection into the crest of the downstream ridge indicates an amplification of the ridge. For the RW case instead, negative PV advection peaks on the western flank of the downstream ridge and opposes this way the positive PV advection through $\mathbf{v}_{\psi\text{midlat}}$ (Fig. 10c). This indicates a deceleration of the eastward progression of the upstream trough and an intensification of the midlatitude jet in this region. The latter interpretation is confirmed by the composite of ageostrophic geopotential flux convergence. The upper-level divergent winds to the northwest of the TC cause ageostrophic fluxes that are directed upstream. These fluxes converge with downstream-directed ageostrophic fluxes associated with the developing baroclinic wave. According to Eq. (3), this ageostrophic geopotential flux convergence on the western flank of the downstream ridge results in an accumulation of eddy kinetic energy (i.e., an intensification of the midlatitude jet). The ageostrophic geopotential flux convergence is weaker in the no-RW case possibly due to a less pronounced upstream trough and therefore less intense ageostrophic geopotential fluxes (Fig. 12d). This difference between the two cases at early stages of the TC–midlatitude flow interaction might reveal the importance of the upstream trough for the further downstream development.

A TC centered dipole pattern of PV advection through the anticyclonic flow of the downstream ridge indicates a northward movement of the TC relative to the basic flow (Fig. 10c), which might contribute to a phase locking between the upstream trough and the TC. This would coincide with findings in idealized studies, which suggested that midlatitude circulation anomalies induce a flow that attracts the TC (Scheck et al. 2011a,b).

d. Dynamics of RW and no-RW cases 2 days after recurvature

The differences between the two cases become most evident 2 days after recurvature. In the RW case, the TC is located directly to the east of the midlatitude upstream trough (Fig. 14a). The upper-level PV structure shows the amplification of a downstream ridge–trough couplet over the central North Pacific as part of the downstream development (see also supplemental Fig. S1). In the no-RW case, the TC is weaker and located farther from the less pronounced upper-level

---

[1] It should be noted here that the QG assumption does not hold true in regions of strong curvature since geostrophic balance neglects centrifugal forces. The geostrophic wind overestimates the nondivergent wind for cyclonic curvature (e.g., TC; base of a trough) and underestimates the nondivergent wind for anticyclonic curvature (e.g., crest of a ridge). Thus, QG vertical motion tends to be too high (low) in regions with cyclonic (anticyclonic) curvature (e.g., Moore and Vanknowe 1992).
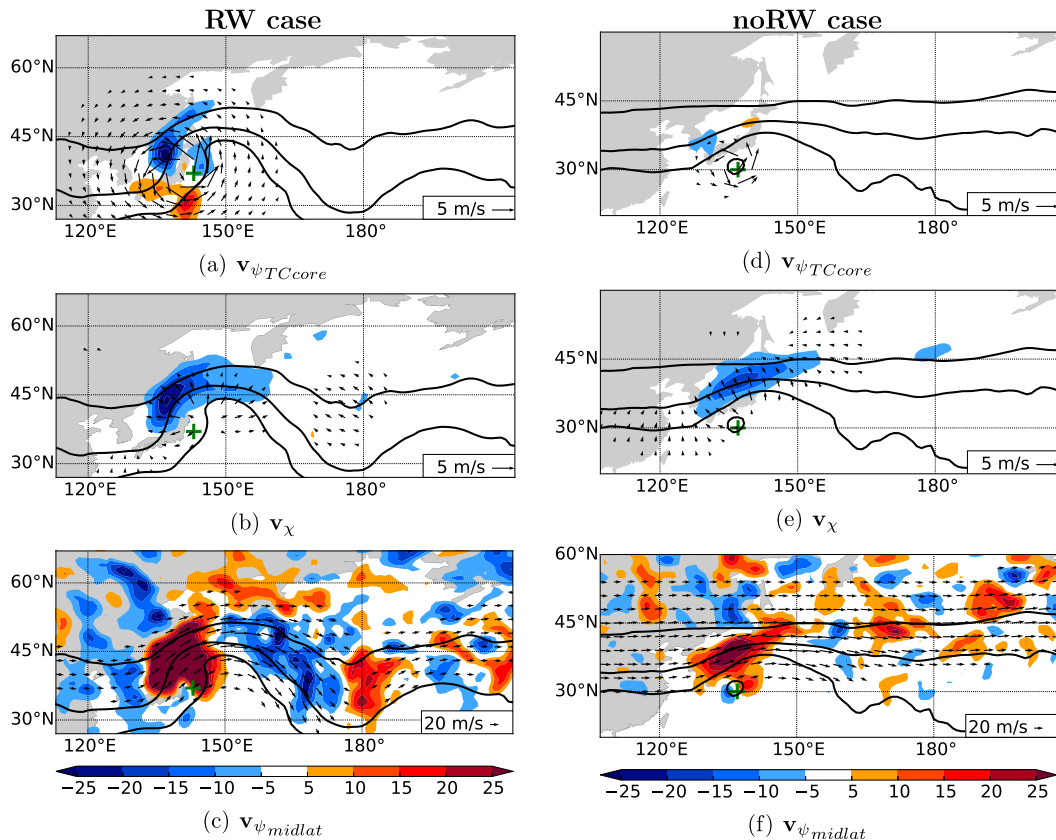
FIG. 14. As in Fig. 10, but 2 days after recurvature.

trough (Fig. 14d). Except for the weak downstream ridge, the midlatitude flow is rather zonally oriented.

In the RW case, the PV structure and the advection patterns indicate that the cyclonic circulation of the developing ET system contributes to the wrap up of the upstream trough (Fig. 14a). Upper-level PV (supplemental Fig. S1) as well as upper-level relative vorticity (supplemental Fig. S2) indicate that the former TC core has connected with the upstream trough and thus cannot be clearly distinguished from the midlatitude flow. Thus, the upper-level cyclonic wind field and the dipole in PV advection in Fig. 14a is presumably a result of both the inner core circulation of the ET system and the cyclonic circulation of the approaching upper-level trough. Nevertheless, because of to the proximity of the transitioning TC to the midlatitude waveguide we assume that the inner core circulation has a considerably stronger impact on the midlatitude flow than at recurvature time. In the no-RW case, $\mathbf{v}_{\psi TC}$ does not show a significant contribution to the PV advection (Fig. 14d). An analysis of the mean relative vorticity in a radius of 600 km around the TC center shows that the upper-level vorticity of the RW case

TCs is significantly stronger than the upper-level vorticity of the no-RW case TCs (not shown). Hence, the differences in the PV advection through $\mathbf{v}_{\psi TC}$ can be attributed to a relatively weak upper-level cyclonic anomaly in the no-RW case.

The upper-level divergent flow contributes to an amplification of the downstream ridge and an intensification of the midlatitude jet. The lower- to midtropospheric ascent has intensified compared to recurvature time (Figs. 15a,d). The strongest vertical motion occurs to the north and northeast of the transitioning TC and along the midlatitude baroclinic zone which is deflected northward (southward) to the east (west) of the TC (see supplemental Fig. S3 for full evolution). The ascent can be attributed to QG forcing both from the upstream trough (Figs. 15b,e, and supplemental Fig. S4) and the interaction of the low-level circulation with the baroclinic zone (Figs. 15c,f, and supplemental Fig. S4). The low-level QG forcing indicates the change from a barotropic to a rather baroclinic system: low-level forced QG ascent is suggestive of warm air advection at low levels due to the interaction of the cyclonic wind field of the TC and the midlatitude
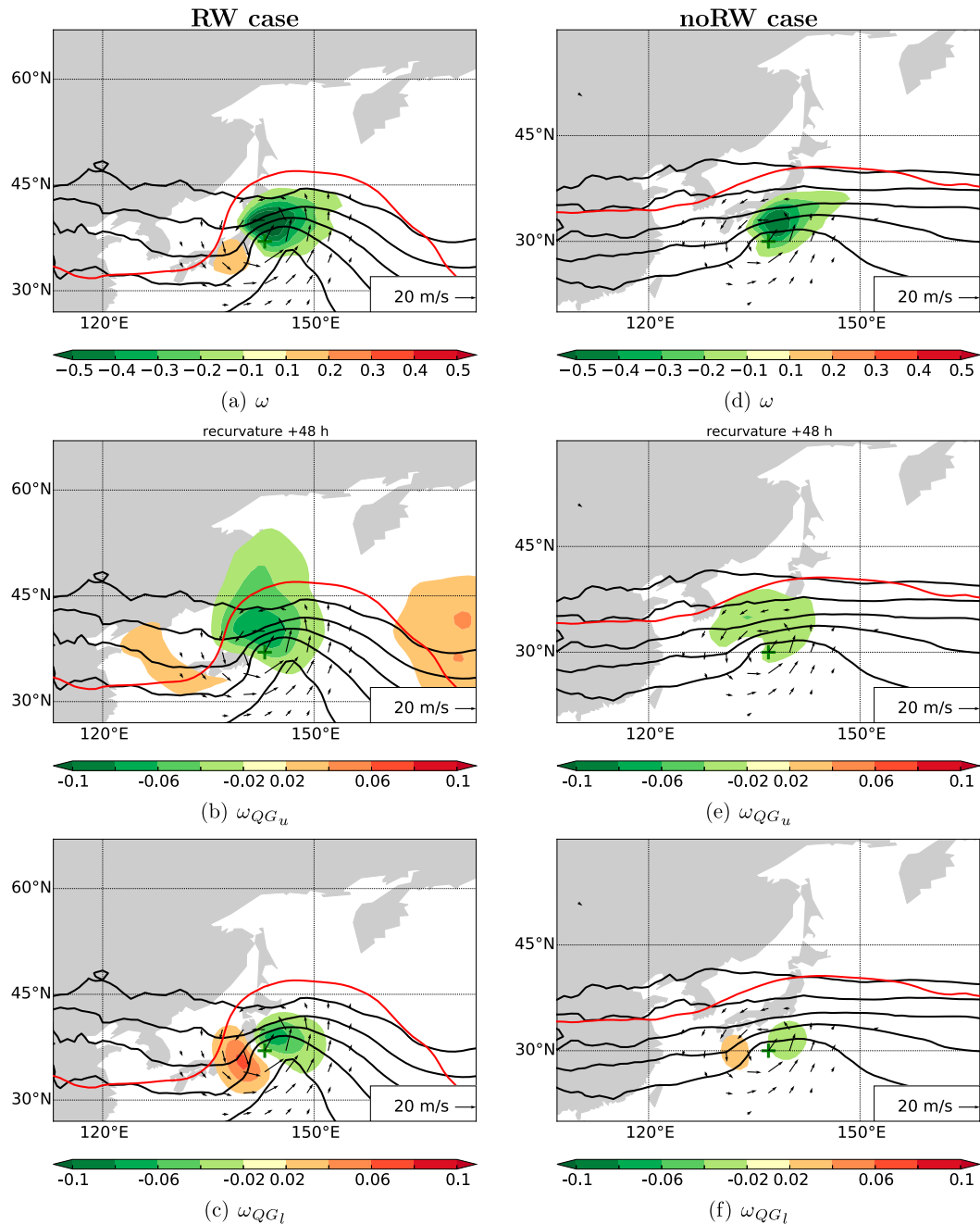
FIG. 15. As in Fig. 11, but showing 700–500-hPa (a),(d) total vertical velocity (shading in Pa s^{-1}); (b),(e) QG vertical velocity forced from upper troposphere (500–100 hPa); and (c),(f) QG vertical velocity forced from lower troposphere (1000–750 hPa) 2 days after recurvature. Note the different color bar used for (a) and (d).

baroclinic zone. In addition, this interaction leads to cold air advection, which forces descent to the west of the transitioning TC. For the RW case, the total vertical motion (Fig. 15a) is approximately 4 times larger than that associated with QG forcing, but the spatial pattern is similar. This indicates that the vertical motion is driven by the synoptic-scale forcing and significantly

enhanced by diabatic processes. A similar picture is obtained for the no-RW case, but at much weaker amplitude. Note that the interaction of the TC with the midlatitude flow contributes to an enhanced QG forcing in the RW case. The upper-level divergent flow can thus no longer be described as the outflow from the TC. It rather arises due to the interaction between the TC and
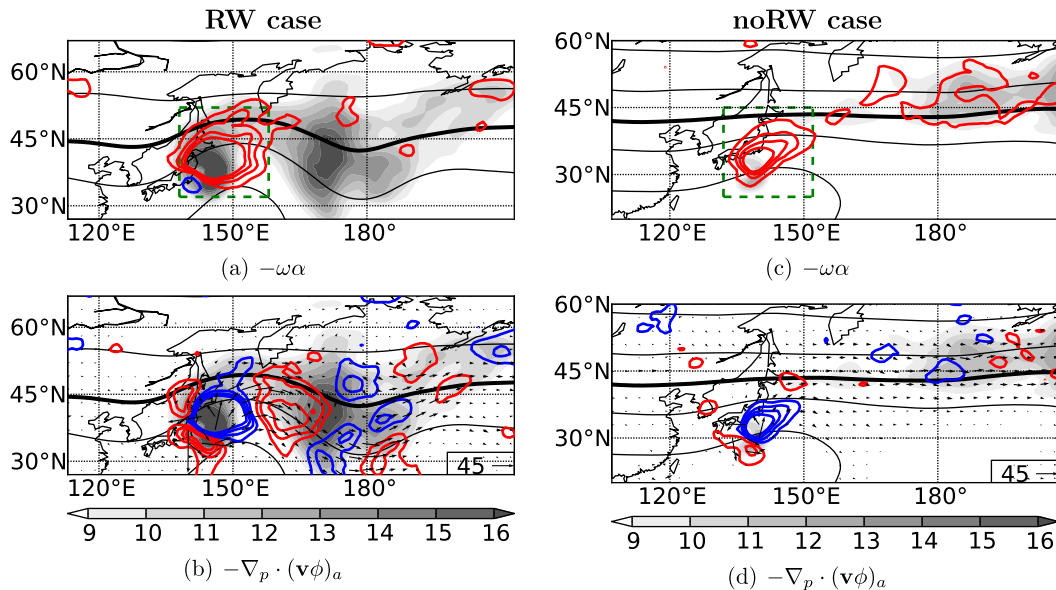
FIG. 16. As in Fig. 12, but 2 days after recurvature.

the midlatitude flow. Our analysis indicates that the vertical motion and thus the upper-level divergent flow arise due to the combination of synoptic-scale forcing and diabatic enhancement. The negative PV advection through the divergent wind is stronger than at recurvature (Figs. 14b,e). The resulting amplification of the upper-level wave pattern is markedly stronger for the RW case.

The enhanced vertical motion results in increased baroclinic conversion in both cases (Figs. 16a,c). The average of baroclinic conversion over the $20° \times 20°$ box is significantly stronger in the RW case than in the no-RW case (Fig. 13, Table 2). The contribution of QG ascent to the baroclinic conversion increased in the RW case as well as in the no-RW case. The QG ascent accounts for about 34% (28%) of the total baroclinic conversion in the RW (no-RW) case composite (Table 2). Similar to recurvature time, upper-level forced ascent dominates the QG contribution to the baroclinic conversion with 27% and 24%, respectively (see also Figs. 15b,e and supplemental Fig. S4). The increase of the QG vertical motion and its contribution to baroclinic conversion reveals a synergistic interaction between the TC and the midlatitude flow. The amplified midlatitude flow provides stronger upper-level forcing that helps to maintain the strength of the upper-level divergent flow and the intensity of the transitioning TC (cf. Fig. 19a). The region of strongest baroclinic conversion is superposed by ageostrophic geopotential flux divergence (Figs. 16b,d). This divergence and northward directed ageostrophic geopotential fluxes indicate the dispersion

of locally generated K_e into midlatitudes. In the RW case, ageostrophic geopotential flux convergence on the flanks of the downstream ridge represents the accumulation of K_e and a further amplification of the wave. A comparison of the vertically integrated K_e on the eastern flank of the downstream ridge at recurvature time (Fig. 12b) and 2 days after recurvature (Fig. 16b) shows the remarkable increase of K_e. It should be mentioned here that the vertically integrated K_e in the vicinity of the transitioning TC increased as well. Thus, some of the baroclinically produced K_e is not dispersed into midlatitudes, but accumulated around the TC.

To assess the importance of QG vertical motion for the wave amplification from a PV perspective, we compute the divergence related to the QG ascent ω_{QG} via the continuity equation on pressure levels ($\partial u/\partial x + \partial v/\partial y = -\partial \omega_{QG}/\partial p$). The successive overrelaxation (section 2d) allows us to retrieve the corresponding divergent wind field. The negative PV advection through this divergent wind field (Fig. 17) is much weaker than the negative PV advection through $\mathbf{v}_\chi$

TABLE 2. As in Table 1, but for 2 days after recurvature. The box over which the average was performed is shown in Fig. 16.

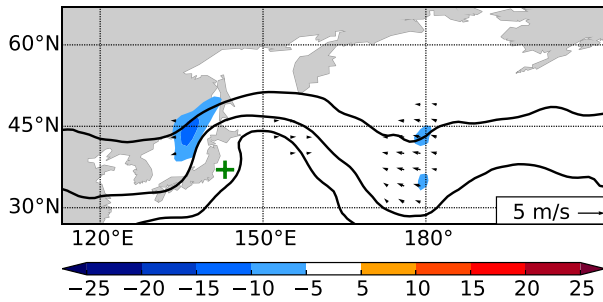|	Confidence level	RW case	No-RW case
$\omega_{QG_l}\alpha/\omega\alpha$ (%)		7	4
$\omega_{QG_u}\alpha/\omega\alpha$ (%)		27	24
$\omega_{QG}\alpha/\omega\alpha$ (%)		34	28
$\omega_{QG}\alpha$ (W m^{-2})	99.9%	8.2	2.7
$\omega\alpha$ (W m^{-2})	99.9%	23.9	9.9

FIG. 17. As in Fig. 14b, but negative PV advection by divergent wind forced through QG vertical motion.

(Fig. 14b). Thus, upper-level divergence associated with diabatic vertical motion likely dominates the negative PV advection. Interestingly, the upper-level divergence associated with QG vertical motion plays a more important role ahead of the downstream trough. Here, the divergent wind through QG vertical motion reaches on average a similar magnitude as the full divergent wind. This difference between the QG contributions to upper-level divergence in the vicinity of the transitioning TC and ahead of the downstream trough points to the importance of diabatically driven vertical motion during TC–midlatitude flow interactions.

The PV advection through the upper-level divergent flow (Fig. 14b) and through $\mathbf{v}_{\psi \text{TC}}$ (Fig. 14a) opposes positive PV advection through $\mathbf{v}_{\psi \text{midlat}}$ (Fig. 14c). This still indicates a deceleration of the eastward propagation of the Rossby wave. However, the PV advection through the divergent wind and $\mathbf{v}_{\psi \text{TC}}$ does not fully compensate the positive PV advection

through $\mathbf{v}_{\psi \text{midlat}}$ so that we expect a net eastward propagation of the wave.

e. Characteristics of the TCs after recurvature

The composites (Figs. 10, 14, and supplemental Fig. S1) suggest that the TCs in the RW case and no-RW case follow different tracks after recurvature. A comparison of the best tracks in a recurvature-relative framework confirms this impression. Most of the TCs in the no-RW case make a sharp recurvature and move in easterly directions due to a strong zonal flow (Fig. 18b). In the RW case, most of the TC tracks exhibit a stronger meridional component and cross the midlatitude waveguide (Fig. 18a). This indicates that in the case of a Rossby wave development the TC is locked with the midlatitude meridional flow of the upstream trough. According to the track behavior after recurvature, the RW case TCs would correspond to TCs that recurve in a northwest pattern (Harr et al. 2000, their Fig. 2) and undergo ET as a seclusion-occlusion type (Kitabatake 2008, their Fig. 3). The no-RW case TCs would correspond to TCs that undergo ET as an open-wave or cold advection type.

The QG forcing diagnostics and the midlatitude flow structure indicate that the TCs enter a region of upper-level forcing after recurvature. This suggests that the TCs may keep their intensity or that they may even reintensify as an extratropical low pressure system. To investigate a potential impact of the midlatitude flow configuration on the transitioning TCs we investigate their intensity and intensity change at the time when the TCs were first classified as an extratropical cyclone.
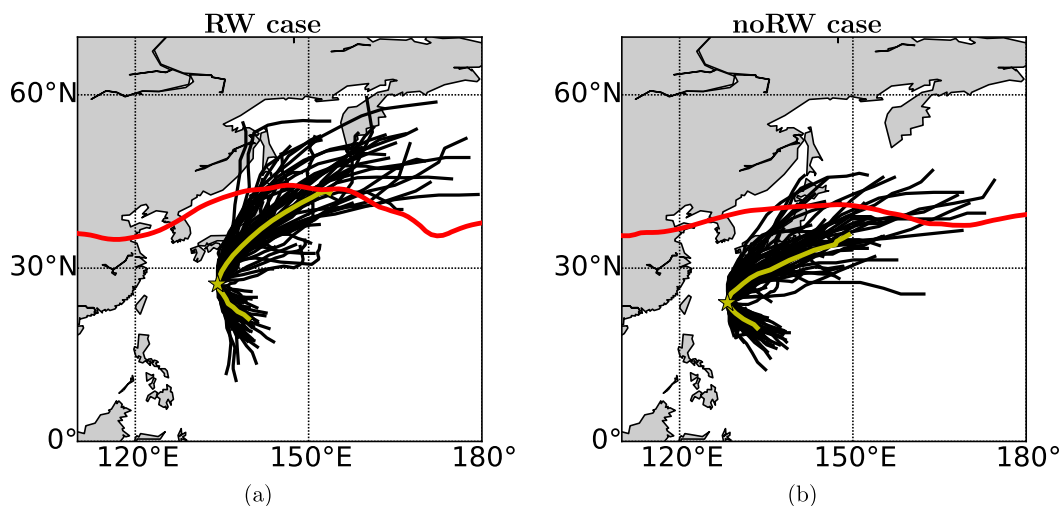

FIG. 18. 320–360-K PV (contoured in red at 2 PVU) and best tracks of (a) the RW case TCs and (b) the no-RW case TCs in a recurvature-relative framework. The yellow line gives the mean recurving track ($T - 48$ to $T + 96$ h) and the yellow star denotes the mean recurvature point. For illustrative purposes the coastlines are shown relative to the mean TC position at recurvature time.
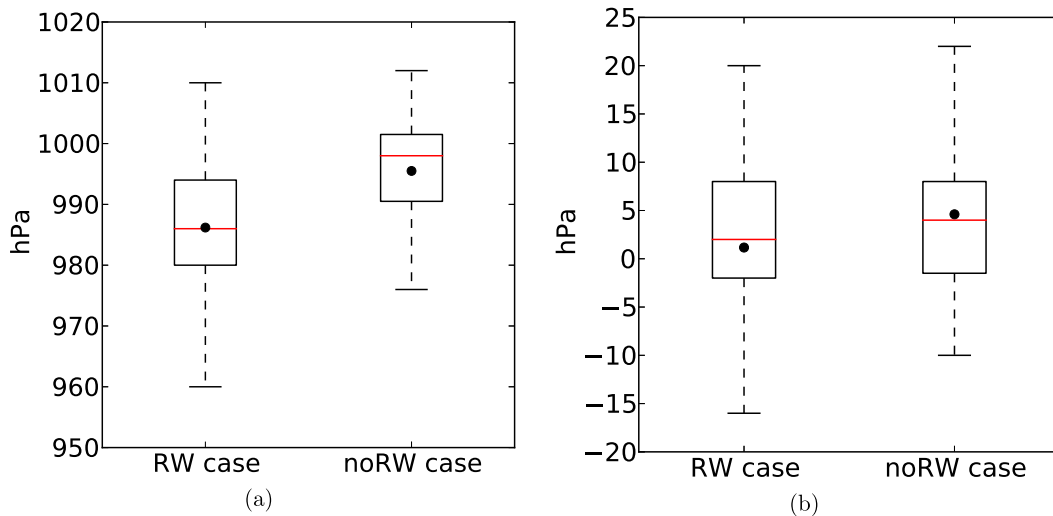
FIG. 19. As in Fig. 9, but for the (a) mean sea level pressure (hPa) at the time when the RW case TCs and no-RW case TCs were first classified as extratropical cyclone and the (b) mean sea level pressure change (hPa) between the time of classification as extratropical cyclone and the end of the best track.

With a mean sea level pressure of 986 hPa, the RW case TCs are significantly more intense at the 99.9% confidence level than the no-RW case TCs, which exhibit a mean sea level pressure of about 995 hPa (Fig. 19a). The mean sea level pressure change between the time of the classification as an extratropical cyclone and the end of the best track do not differ significantly between the RW case and no-RW case TCs (Fig. 19b). The average mean sea level pressure change is about +1 hPa for the RW case TCs and +5 hPa for the no-RW case TCs (i.e., on average the TCs weaken after the classification as an extratropical cyclone).

The differences between the RW and no-RW case synoptic setup suggest that the inner-core structure of the TCs might evolve differently during ET. To investigate the structural changes during ET, we computed the cyclone phase space parameters (Hart 2003) for the composite RW and no-RW case TCs from 1 day prior to recurvature to 3 days after recurvature. These parameters are the 900–600-hPa storm-relative thickness symmetry B, the 900–600-hPa thermal wind $-V_T^L$, and the 600–300-hPa thermal wind $-V_T^U$. The RW case TCs as well as no-RW case TCs develop from a deep symmetric warm-core cyclone into an asymmetric warm-core cyclone and finally into a deep asymmetric cold-core system (Figs. 20a,b). For both cases, the onset of ET ($B > 10$ m; Evans and Hart 2003) occurs 18–30 h after recurvature and the completion of ET ($-V_T^L < 0$) occurs 42–48 h after recurvature. However, the asymmetry develops much more rapidly for the RW case TCs than for the no-RW case TCs. While B reaches values of more than 30 m for the RW case TCs 48 h after

recurvature, the no-RW case TCs exhibit a storm-relative thermal symmetry of about 15 m at the same time. This indicates that frontal features develop more rapidly for the RW case TCs. The symmetry of the no-RW case TCs reaches similar values 72 h after recurvature. The evolution of the upper-level thermal wind parameter $-V_T^U$ exhibits similar characteristics for the RW and no-RW case TCs (not shown).

5. Predictability downstream of recurving TCs

The adequate representation of the synergistic TC–midlatitude flow interaction may pose a challenge for numerical weather prediction systems. On the one hand, an inadequate representation of the influence of the midlatitude flow on the TC may lead to forecast errors concerning the structural changes within the TC (Evans et al. 2006). On the other hand, the incorrect representation of the TC–midlatitude flow interaction may cause forecast errors and uncertainties along the waveguide (e.g., McTaggart-Cowan et al. 2007; Pantillon et al. 2013). These forecast errors and uncertainties associated with recurving TCs tend to spread into downstream regions with a midlatitude Rossby wave and lead to a reduced predictability (Anwender et al. 2008; Harr et al. 2008; Reynolds et al. 2009; Anwender et al. 2010; Pantillon et al. 2013; Aiyyer 2015). Given the results of this study and the studies by Archambault et al. (2015) and Torn and Hakim (2015), Rossby waves that are associated with a recurving TC may cause an enhanced forecast uncertainty in downstream regions from a climatological perspective. We hypothesize further that
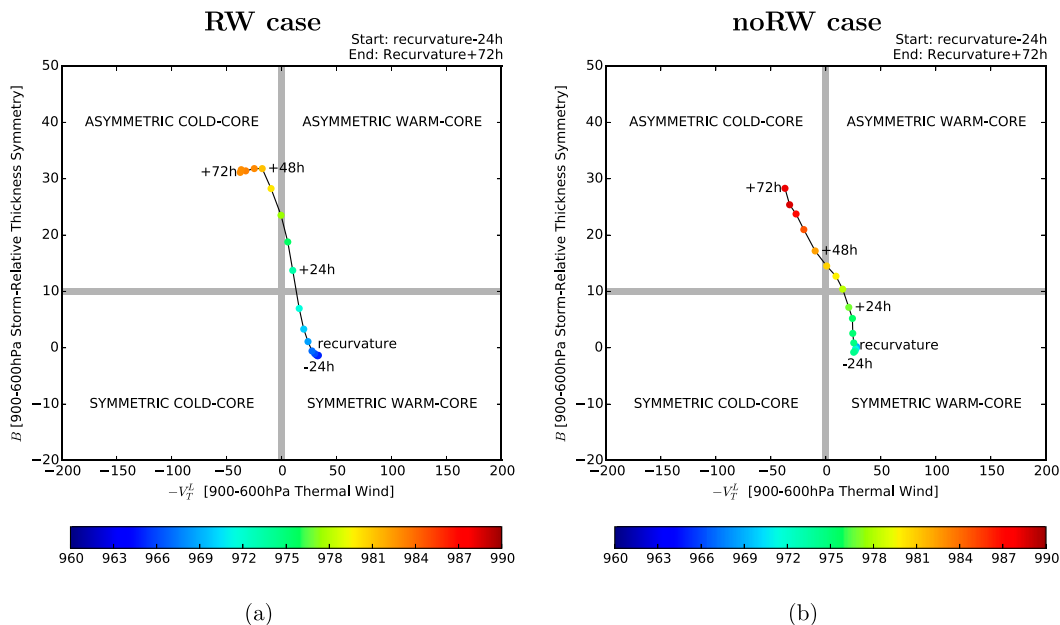
FIG. 20. Cyclone phase space diagram for the (a) RW case TC and (b) the no-RW case TC from 1 day prior to recurvature to 3 days after recurvature. Phase evolution of $-V_T^L$ versus B. A marker is placed every 6 h. The color of each marker denotes the cyclone mean sea level pressure (hPa) according to the best track data.

the propagation of forecast uncertainty differs between cases with and without downstream Rossby wave development.

To test these hypotheses, we investigate NOAA's second-generation GEFS reforecast data (Hamill et al. 2013) downstream of recurving WNP TCs. The reforecast dataset consists of an 11-member ensemble of forecasts that is run daily from 0000 UTC initial conditions with a horizontal resolution of 0.5°. We investigate the standard deviation of 192-h, 250-hPa geopotential height forecasts that were initialized closest to recurvature time of all WNP TCs during June–November 1985–2010. During this period, 231 TCs fulfilled the recurvature criteria given in section 2a. A total of 48 TCs were identified as RW and no-RW case TCs, respectively. In the following we present noncentered Hovmöller composites of anomalies of standard deviation averaged between 20° and 80°N relative to the June–November 1985–2010 climatology. The significance of the anomalies is determined using a Monte Carlo approach (section 2c).

Ensemble forecasts that were initialized closest to recurvature time show a statistically significant positive anomaly of ensemble spread downstream of WNP recurving TCs (Fig. 21). The spread starts to increase over the WNP about 2 days after recurvature and reaches a local maximum 6 days after recurvature over the central North Pacific. A second local maximum of ensemble spread starts to develop over western North

America about 3–4 days after recurvature. The local maximum propagates downstream and reaches central North America about 8 days after recurvature. A third region of enhanced ensemble spread starts to develop 6 days after recurvature over the North Atlantic.

The set of RW and no-RW cases allows us to examine the importance of a developing Rossby wave for the downstream propagation of forecast uncertainty. The
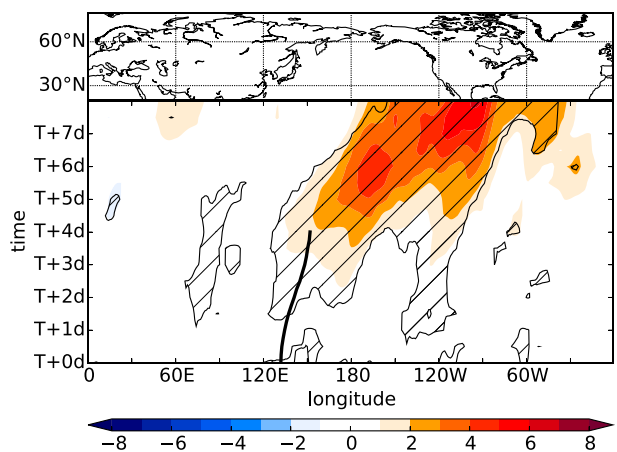

FIG. 21. Recurvature-relative composites of the anomaly of 250-hPa geopotential height ensemble standard deviation (shaded in gpm) relative to June–November climatology for WNP TCs. Values that are statistically significant at the 95% confidence level are hatched. Black thick line gives the mean recurving track ($T + 0$ to $T + 96$ h).
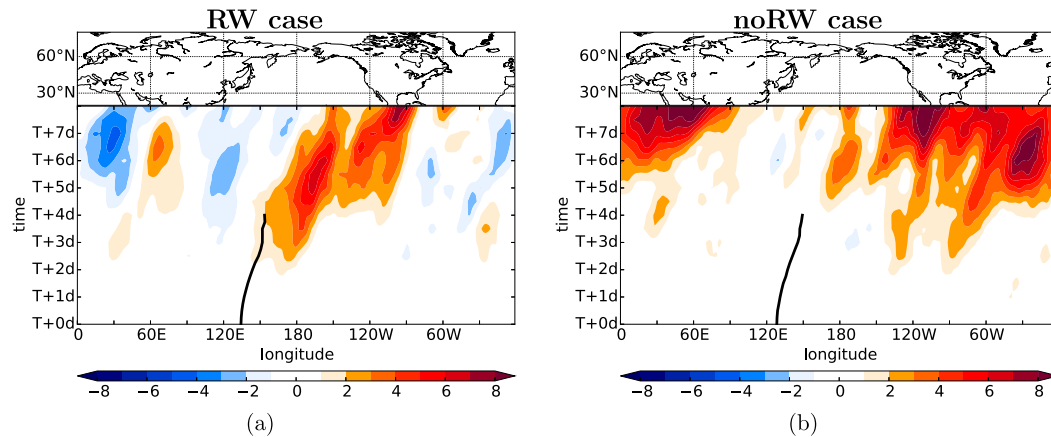
FIG. 22. Recurvature-relative composites of the anomaly of 250-hPa geopotential height ensemble standard deviation (shaded in gpm) relative to June–November climatology for WNP (a) RW case and (b) no-RW case TCs. Black thick line gives the mean recurving track ($T + 0$ to $T + 96$ h).

evolution of forecast uncertainty in the RW case (Fig. 22a) is quite similar to the evolution downstream of all WNP TCs (Fig. 21). The ensemble spread starts to increase 2 days after recurvature over the WNP. A region of enhanced forecast uncertainty propagates with the phase velocity of the Rossby wave into the eastern North Pacific. A second region of enhanced forecast uncertainty develops 4 days after recurvature over the eastern North Pacific and propagates with phase velocity into central North America. For the no-RW case TCs, the evolution of forecast uncertainty is very different (Fig. 22b). A positive anomaly of forecast uncertainty over the central North Pacific 5 days after recurvature is presumably related to the recurving TCs. However, this locally enhanced forecast uncertainty does not propagate into downstream regions with a RWP. Instead, anomalously high forecast uncertainty, which is potentially not related to the recurving TCs develops between North America and the Eurasian continent 4–5 days after recurvature time. This increase might be due to the rather zonal midlatitude flow configuration over the North Pacific during the occurrence of no-RW cases. Grazzini and Vitart (2015) showed that rather zonal flow configurations over the North Pacific tend to be associated with enhanced forecast uncertainty over the European region compared to situations with RWP activity over the North Pacific. The ensemble reforecast dataset provides a great opportunity for future research concerning the midlatitude forecast uncertainty associated with TCs. The identification of configurations that favor the development of high forecast uncertainties downstream of recurving TCs would be an intriguing research project. We anticipate that much of the forecast uncertainty in downstream regions is related to the phasing

between a TC and the midlatitude flow (Grams et al. 2013b, 2015).

Finally, we investigate the evolution of ensemble spread downstream of recurving North Atlantic and south Indian Ocean TCs. A total of 113 North Atlantic and 93 south Indian Ocean TCs fulfilled the criteria given in section 2a between June–November 1985–2010 and December–April 1985–2010, respectively. Anomalously high ensemble spread starts to develop immediately downstream of North Atlantic TCs 2 days after recurvature (Fig. 23a). The signature of enhanced ensemble spread propagates with phase velocity toward western Europe. A second region of enhanced ensemble spread evolves about 6 days after recurvature over the Asian continent. These results nicely reveal that although North Atlantic TCs are not associated with a statistically significant increase in RWP frequency and amplitude downstream, they may still impact downstream regions through enhanced forecast uncertainty.

A statistically significant positive anomaly of ensemble spread can be also found downstream of recurving south Indian Ocean TCs (Fig. 23b). The eastward propagation of the positive ensemble spread anomaly shows similarities to the propagation downstream of WNP and North Atlantic TCs. However, farther downstream and upstream of the recurving TCs the ensemble spread is reduced compared to climatology, indicating a higher level of forecast skill. A possible explanation might be that the recurvature of south Indian Ocean TCs occurs during situations with an enhanced Rossby wave activity that are associated with a generally higher intrinsic predictability (Grazzini and Vitart 2015). This higher intrinsic predictability is then locally reduced by the recurving TC. The investigation
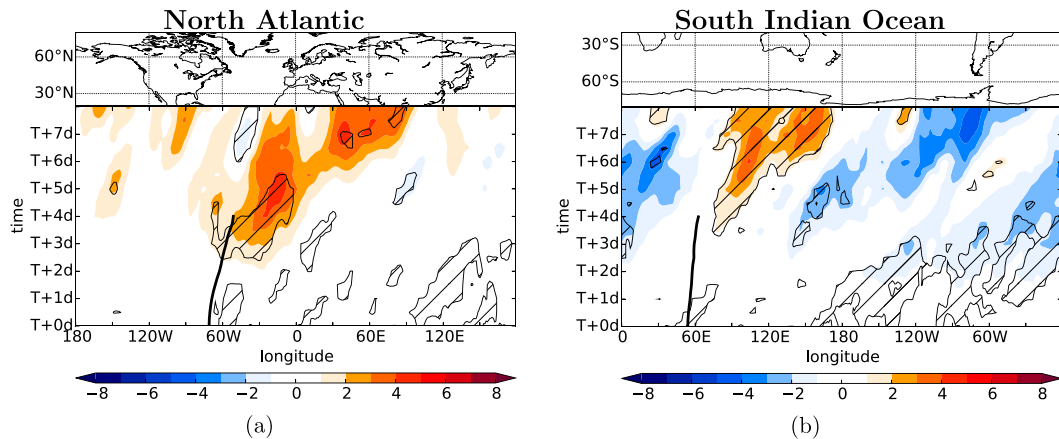
FIG. 23. As in Fig. 21, but for (a) North Atlantic and (b) south Indian Ocean TCs relative to June–November and December–April climatology, respectively.

of this speculation and a more thorough analysis of the substantial ensemble information could be a research opportunity for future studies.

6. Summary and discussion

This study presents a climatological investigation of the impact of recurving TCs on midlatitude RWPs. We identify synoptic-scale RWPs that occurred from 7 days prior to 10 days after recurving TCs in three ocean basins during the period 1980–2010. The RWPs are identified via a Hilbert transform of the meridional wind at 250 hPa (Zimin et al. 2003). This method enables us to identify RWPs as objects so that we can determine their frequency and amplitude.

In the period June–November 1980–2010, 280 TCs recurved and interacted with the midlatitudes over the WNP. The results reveal a significant modification of the midlatitude flow downstream of these TCs (Figs. 3 and 4), which is consistent with results of climatological studies by Archambault et al. (2013, 2015) and Torn and Hakim (2015). In a framework relative to the time when the TCs were first classified as an extratropical cyclone by the responsible RSMC, the RWP amplitude exhibits anomalies of up to $2\,\mathrm{m\,s^{-1}}$ over large portions of the North Pacific (Fig. 4b). This anomaly corresponds to a relative increase of about 30% compared to climatology. The statistical significance of the results indicates that RWPs downstream of recurving TCs are stronger than those that generally occur in midlatitudes. Analogous to the studies by Archambault et al. (2015) and Torn and Hakim (2015), the amplitude of RWPs downstream of WNP TCs decays over North America. A major difference between this study and the studies by Archambault et al. (2015) and Torn and Hakim (2015) is the

compilation of the composites and the statistical evaluation. The phase elimination of the meridional wind through the Hilbert transform allows us to not composite the data on a central longitude. This way, the TC relative composites of RWP amplitude are not enhanced artificially compared to the spatially noncentered and randomly chosen composites incorporated in the Monte Carlo approach. The fact that using a more restrictive spatially noncentered compositing technique yields statistically significant results close to the studies by Archambault et al. (2015) and Torn and Hakim (2015) supports the statement by Archambault et al. (2015) that recurving TCs may contribute importantly to Northern Hemispheric intraseasonal climate variability.

A new outcome of this study is that RWPs occur more frequently downstream of recurving WNP TCs (Figs. 3a and 4a). The RWP frequency exceeds the climatological mean by up to 12% between the WNP and central North America from recurvature time to 7 days after recurvature. In a framework relative to the time when the TCs were first classified as an extratropical cyclone by the responsible RSMC, the RWP frequency anomaly reaches values of up to 20% (Fig. 4). This anomaly corresponds to a relative increase of more than 30% compared to climatology. In addition to their impact on downstream midlatitude dynamics, recurving WNP TCs are a source of forecast uncertainty in downstream regions as shown by a statistically significant anomaly in ensemble standard deviation (Fig. 21). The propagation characteristics of the individual maxima as well as the propagation of the leading edge in ensemble spread suggest that the forecast uncertainty propagates with a RWP into downstream regions.

North Atlantic TCs do not seem to significantly modify RWP frequency and amplitude downstream.

This finding stands in contrast to results of Torn and Hakim (2015) who concluded that RWPs downstream of North Atlantic TCs are significantly weaker than RWPs downstream of August–October extratropical cyclones. The discrepancy between the finding of the Torn and Hakim (2015) study and this study might be related to the different methodological approaches and to different sample sizes. Nevertheless, the signature of the propagation of enhanced ensemble spread suggests that forecast uncertainty associated with recurving North Atlantic TCs propagates into downstream regions with a midlatitude Rossby wave (Fig. 23a). This is consistent with Torn and Hakim (2015) who found a signature of a Rossby wave downstream of North Atlantic ET events. The fact that we do see the signature of a Rossby wave in the ensemble spread, but not in the RWP amplitude and frequency anomalies is not a contradiction. It rather supports the statement made in section 3c that North Atlantic TCs are able to modify RWPs, but that these RWPs do not depart significantly from the general variability of midlatitude RWPs in that region.

South Indian Ocean TCs have a statistically significant impact on RWP frequency and amplitude (Fig. 5). The RWP frequency exceeds the climatological mean by up to 15% between 60°E and 180° from 2 to 7 days after recurvature. This increase corresponds to a relative increase of more than 30% relative to the climatological RWP frequency. Over the same region, the RWP amplitude is enhanced significantly by up to $2 \, \mathrm{m \, s^{-1}}$ (i.e., 20%–30% compared to climatology). The statistical significance of the results indicates that RWPs downstream of recurving south Indian Ocean TCs are stronger than those that generally occur in midlatitudes. Since high-amplitude Rossby waves have been linked to heat waves in southeastern Australia (Parker et al. 2013), south Indian Ocean TCs may impact the development of weather extremes during austral summer and fall. These extremes might be hard to predict as indicated by a statistically significant positive anomaly of ensemble spread downstream of recurving south Indian Ocean TCs (Fig. 23b).

We identify cases with and without Rossby wave development downstream of WNP recurving TCs (supplemental Fig. S1). The two subsets are used to identify favorable conditions for a Rossby wave development in a composite framework. Despite the fact that creating subsets based on the midlatitude flow response is roughly inverse to the approach in Archambault et al. (2015), the subsets of the two studies exhibit very similar characteristics. The results suggest that a precursor Rossby wave that emerges from the Asian continent provides favorable conditions for a downstream development (Fig. 7a). The precursor Rossby wave is strongly amplified during the interaction with the TC that coincides with the findings of Riemer and Jones (2010), Archambault et al. (2015), and Torn and Hakim (2015). They conclude that the interaction of a TC with a precursor Rossby wave leads to a greater downstream response. Interestingly, Torn and Hakim (2015) use an inverse approach to this study by identifying cases with an upstream precursor trough. The fact that two inverse approaches lead to the same conclusions underlines the robustness of the findings. The climatological investigation of ensemble spread for the RW case as well as for the no-RW case reveals the relevance of the Rossby wave development in terms of forecast uncertainty. The development of a Rossby wave in the RW cases allows forecast uncertainty to propagate from the region of the recurving WNP TCs into downstream regions (Fig. 22a). Without Rossby wave amplification, this downstream propagation of forecast uncertainty does not occur (Fig. 22b).

The composite maps clearly depict the existence of an upstream trough in the RW case at recurvature time (Fig. 10a). This synoptic setup strongly resembles the northwest pattern, which provides favorable conditions for an extratropical reintensification (Harr et al. 2000) and for a strong TC–midlatitude flow interaction as defined by the negative PV advection by the upper-level divergent wind (Archambault et al. 2015). The composites presented in this study corroborate the findings of previous studies concerning the importance of the upper-level divergent wind for the midlatitude flow evolution downstream of TCs (e.g., Riemer et al. 2008; Riemer and Jones 2010; Torn 2010; Archambault et al. 2013, 2015). In particular, the synoptic setup for the RW and no-RW cases exhibits strong similarities with the strong and weak TC–midlatitude flow interactions investigated by Archambault et al. (2013, 2015). Negative PV advection through the divergent wind contributes to an amplification of the ridge itself and to an intensification of the midlatitude jet on the western flank of the downstream ridge (Fig. 10b). The results from our composites indicate that the upper-level divergent flow should not be described as being outflow from the TC. It arises through the nonlinear interaction between the TC and the midlatitude flow that leads to a stronger amplification of the upper-level wave pattern and helps to maintain the strength of the transitioning TC. The associated QG forcing of vertical motion is enhanced by diabatic processes, supported by the moisture brought into the system by the strong cyclonic circulation of the transitioning TC.

The accumulation of K_e through ageostrophic geopotential flux convergence on the western flank of the downstream ridge underlines the importance of the

upper-level divergent flow (Fig. 12b). In contrast to the downstream baroclinic development paradigm (Orlanski and Sheldon 1995), the convergence is not solely a result of ageostrophic winds related to troughs and ridges of the developing baroclinic wave. It is a result of ageostrophic winds associated with the upstream trough and the ageostrophic divergent flow related to the nonlinear interaction between the TC and the midlatitude flow. Analogous to the jet intensification through this ageostrophic flux convergence, Archambault et al. (2015) document PV frontogenesis through the upper-level flow on the western flank of the downstream ridge. The PV frontogenesis is more intense in the strong TC–midlatitude flow interaction cases that tend to be associated with a stronger downstream flow response. In addition to the jet intensification and ridge amplification, the upper-level divergent flow impedes the eastward propagation of the upstream trough and enables this way a favorable phasing of the TC with the extratropical flow pattern. The importance of the upper-level divergent flow for the phasing of a transitioning TC and an upstream trough has been documented in several recent studies (e.g., Griffin and Bosart 2014; Pantillon et al. 2015; Archambault et al. 2015). The RW case TCs phase lock with the midlatitude flow on the eastern flank of this trough and follow a northward track (Fig. 18a). The phasing of the TC and the midlatitude flow in the RW cases represents a synergistic interaction (Bosart and Lackmann 1995; Archambault et al. 2015), which becomes apparent in the composites 2 days after recurvature.

The ridge amplification and jet intensification through the upper-level divergent flow is supposed to lead to an increase of QG forced ascent, which may help to maintain the strength of the transitioning TC in a highly baroclinic environment. Best track mean sea level pressure data as well as an increase of K_e even indicate an intensification (Figs. 19a and 16a). From a K_e perspective, strong baroclinic conversion in the vicinity of the transitioning TC contributes to an intensification (Fig. 16a). The contribution of QG vertical motion to the full baroclinic conversion increases from 22% at recurvature time to 34% at 2 days after recurvature (Tables 1 and 2). The QG vertical motion is dominated from upper-level forcing (Figs. 13, 15b, 15e, and supplemental Fig. S4). The relatively small contribution of QG vertical motion to the full baroclinic conversion indicates that diabatically driven vertical motion dominates, which is consistent with Riemer et al. (2014, their Fig. 11a). Both the baroclinic conversion from the model vertical motion and the baroclinic conversion from QG vertical motion are significantly stronger in the RW case than in the no-RW case 2 days after

recurvature (Table 2). Significantly more intense QG forcing for vertical motion was also documented for the strong interaction cases (Archambault et al. 2015, their Fig. 10b). Most of the K_e that is produced through baroclinic conversion in the vicinity of the TC is immediately dispersed into the midlatitude flow where it is accumulated on the eastern flank of the downstream ridge. Thus, in agreement with case studies by Harr and Dea (2009) and Keller et al. (2014), the baroclinic conversion associated with the transitioning TC provides additional K_e and supports the amplification of the downstream midlatitude flow.

Given the facts that recurving TCs impact midlatitude Rossby waves and the downstream predictability, that Rossby waves have been identified as precursors of high-impact weather events (e.g., Martius et al. 2008; Wirth and Eichhorn 2014), and that recurving TCs might occur more frequently over the WNP and the North Atlantic in a changing climate (e.g., Colbert et al. 2013, 2015), accurate forecasts of the TC–midlatitude flow interaction are invaluable. A number of studies indicate that numerical forecast errors result from the inadequate representation of a diabatically driven ridge amplification (e.g., Torn 2010; Rodwell et al. 2013; Gray et al. 2014). Thus, the localization and quantification of analysis and forecast errors in regions where the diabatically driven divergent flow during ET modifies the midlatitude waveguide is planned to be a key aspect of the North Atlantic Waveguide and Downstream Impact Experiment (NAWDEX) field campaign in fall 2016.

the Earth System Research Laboratory. The authors wish to thank three anonymous reviewers for their constructive comments on the manuscript.

REFERENCES

Agusti-Panareda, A., C. D. Thorncroft, G. C. Craig, and S. L. Gray, 2004: The extratropical transition of Hurricane Irene (1999): A potential-vorticity perspective. *Quart. J. Roy. Meteor. Soc.*, **130**, 1047–1074, doi:10.1256/qj.02.140.

Aiyyer, A., 2015: Recurving western North Pacific tropical cyclones and midlatitude predictability. *Geophys. Res. Lett.*, **42**, 7799–7807, doi:10.1002/2015GL065082.

Anwender, D., P. A. Harr, and S. C. Jones, 2008: Predictability associated with the downstream impacts of the extratropical transition of tropical cyclones: Case studies. *Mon. Wea. Rev.*, **136**, 3226–3247, doi:10.1175/2008MWR2249.1.

——, S. C. Jones, M. Leutbecher, and P. A. Harr, 2010: Sensitivity experiments for ensemble forecasts of the extratropical transition of Typhoon Tokage (2004). *Quart. J. Roy. Meteor. Soc.*, **136**, 183–200, doi:10.1002/qj.527.

Archambault, H. M., L. F. Bosart, D. Keyser, and J. M. Cordeira, 2013: A climatological analysis of the extratropical flow response to recurving western North Pacific tropical cyclones. *Mon. Wea. Rev.*, **141**, 2325–2346, doi:10.1175/MWR-D-12-00257.1.

——, D. Keyser, L. F. Bosart, C. A. Davis, and J. M. Cordeira, 2015: A composite perspective of the extratropical flow response to recurving western North Pacific tropical cyclones. *Mon. Wea. Rev.*, **143**, 1122–1141, doi:10.1175/MWR-D-14-00270.1.

Atallah, E. H., and L. F. Bosart, 2003: The extratropical transition and precipitation distribution of Hurricane Floyd (1999). *Mon. Wea. Rev.*, **131**, 1063–1081, doi:10.1175/1520-0493(2003)131<1063:TETAPD>2.0.CO;2.

Bosart, L. F., and G. M. Lackmann, 1995: Postlandfall tropical cyclone reintensification in a weakly baroclinic environment: A case study of Hurricane David (September 1979). *Mon. Wea. Rev.*, **123**, 3268–3291, doi:10.1175/1520-0493(1995)123<3268:PTCRIA>2.0.CO;2.

Boettcher, M., and H. Wernli, 2011: Life cycle study of a diabatic Rossby wave as a precursor to rapid cyclogenesis in the North Atlantic: Dynamics and forecast performance. *Mon. Wea. Rev.*, **139**, 1861–1878, doi:10.1175/2011MWR3504.1.

Burroughs, L. D., and S. Brand, 1973: Speed of tropical storms and typhoons after recurvature in the western North Pacific Ocean. *J. Appl. Meteor.*, **12**, 452–458, doi:10.1175/1520-0450(1973)012<0452:SOTSAT>2.0.CO;2.

Clough, S. A., C. S. A. Davitt, and A. J. Thorpe, 1996: Attribution concepts applied to the omega equation. *Quart. J. Roy. Meteor. Soc.*, **122**, 1943–1962, doi:10.1002/qj.49712253610.

Colbert, A. J., B. J. Soden, G. A. Vecchi, and B. P. Kirtman, 2013: The impact of anthropogenic climate change on North Atlantic tropical cyclone tracks. *J. Climate*, **26**, 4088–4095, doi:10.1175/JCLI-D-12-00342.1.

——, ——, and B. P. Kirtman, 2015: The impact of natural and anthropogenic climate change on western North Pacific tropical cyclone tracks. *J. Climate*, **28**, 1806–1823, doi:10.1175/JCLI-D-14-00100.1.

Cordeira, J. M., and L. F. Bosart, 2010: The antecedent large-scale conditions of the "Perfect Storms" of late October and early November 1991. *Mon. Wea. Rev.*, **138**, 2546–2569, doi:10.1175/2010MWR3280.1.

Dacre, H. F., and S. L. Gray, 2009: The spatial distribution and evolution characteristics of North Atlantic cyclones. *Mon. Wea. Rev.*, **137**, 99–115, doi:10.1175/2008MWR2491.1.

Dee, D. P., and Coauthors, 2011: The ERA-Interim reanalysis: Configuration and performance of the data assimilation system. *Quart. J. Roy. Meteor. Soc.*, **137**, 553–597, doi:10.1002/qj.828.

Deveson, A. C., K. A. Browning, and T. D. Hewson, 2002: A classification of FASTEX cyclones using a height-attributable quasi-geostrophic vertical-motion diagnostic. *Quart. J. Roy. Meteor. Soc.*, **128**, 93–117, doi:10.1256/00359000260498806.

Evans, J. L., and R. E. Hart, 2003: Objective indicators of the life cycle evolution of extratropical transition for Atlantic tropical cyclones. *Mon. Wea. Rev.*, **131**, 909–925, doi:10.1175/1520-0493(2003)131<0909:OIOTLC>2.0.CO;2.

——, J. M. Arnott, and F. Chiaromonte, 2006: Evaluation of operational model cyclone structure forecasts during extratropical transition. *Mon. Wea. Rev.*, **134**, 3054–3072, doi:10.1175/MWR3236.1.

Glatt, I., and V. Wirth, 2014: Identifying Rossby wave trains and quantifying their properties. *Quart. J. Roy. Meteor. Soc.*, **140**, 384–396, doi:10.1002/qj.2139.

——, A. Dörnbrack, S. Jones, J. Keller, O. Martius, A. Müller, D. H. W. Peters, and V. Wirth, 2011: Utility of Hovmöller diagrams to diagnose Rossby wave trains. *Tellus*, **63A**, 991–1006, doi:10.1111/j.1600-0870.2011.00541.x.

Grams, C. M., and S. R. Blumer, 2015: European high impact weather downstream of Hurricane Katia (2011) undergoing extratropical transition. *Geophys. Res. Lett.*, **42**, 8738–8748, doi:10.1002/2015GL066253.

——, and Coauthors, 2011: The key role of diabatic processes in modifying the upper-tropospheric wave guide: A North Atlantic case-study. *Quart. J. Roy. Meteor. Soc.*, **137**, 2174–2193, doi:10.1002/qj.891.

——, S. C. Jones, C. A. Davis, P. A. Harr, and M. Weissmann, 2013a: The impact of Typhoon Jangmi (2008) on the midlatitude flow. Part I: Upper-level ridgebuilding and modification of the jet. *Quart. J. Roy. Meteor. Soc.*, **139**, 2148–2164, doi:10.1002/qj.2091.

——, ——, and ——, 2013b: The impact of Typhoon Jangmi (2008) on the midlatitude flow. Part II: Downstream evolution. *Quart. J. Roy. Meteor. Soc.*, **139**, 2165–2180, doi:10.1002/qj.2119.

——, S. T. K. Lang, and J. H. Keller, 2015: A quantitative assessment of the sensitivity of the downstream midlatitude flow response to extratropical transition of tropical cyclones. *Geophys. Res. Lett.*, **42**, 9521–9529, doi:10.1002/2015GL065764.

Gray, S. L., C. M. Dunning, J. Methven, G. Masato, and J. M. Chagnon, 2014: Systematic model forecast error in Rossby wave structure. *Geophys. Res. Lett.*, **41**, 2979–2987, doi:10.1002/2014GL059282.

Grazzini, F., and F. Vitart, 2015: Atmospheric predictability and Rossby wave packets. *Quart. J. Roy. Meteor. Soc.*, **141**, 2793–2802, doi:10.1002/qj.2564.

Griffin, K. S., and L. F. Bosart, 2014: The extratropical transition of Tropical Cyclone Edisoana (1990). *Mon. Wea. Rev.*, **142**, 2772–2793, doi:10.1175/MWR-D-13-00282.1.

Hamill, T. M., G. T. Bates, J. S. Whitaker, D. R. Murray, M. Fiorino, T. J. Galarneau, Y. Zhu, and W. Lapenta, 2013: NOAA's Second-Generation Global Medium-Range Ensemble Reforecast Dataset. *Bull. Amer. Meteor. Soc.*, **94**, 1553–1565, doi:10.1175/BAMS-D-12-00014.1.

Harr, P. A., and J. M. Dea, 2009: Downstream development associated with the extratropical transition of tropical cyclones

over the western North Pacific. *Mon. Wea. Rev.*, **137**, 1295–1319, doi:10.1175/2008MWR2558.1.

——, R. L. Elsberry, and T. F. Hogan, 2000: Extratropical transition of tropical cyclones over the western North Pacific. Part II: The impact of midlatitude circulation characteristics. *Mon. Wea. Rev.*, **128**, 2634–2653, doi:10.1175/1520-0493(2000)128<2634:ETOTCO>2.0.CO;2.

——, D. Anwender, and S. C. Jones, 2008: Predictability associated with the downstream impacts of the extratropical transition of tropical cyclones: Methodology and a case study of Typhoon Nabi (2005). *Mon. Wea. Rev.*, **136**, 3205–3225, doi:10.1175/2008MWR2248.1.

Hart, R. E., 2003: A cyclone phase space derived from thermal wind and thermal asymmetry. *Mon. Wea. Rev.*, **131**, 585–616, doi:10.1175/1520-0493(2003)131<0585:ACPSDF>2.0.CO;2.

Hodyss, D., and E. Hendricks, 2010: The resonant excitation of baroclinic waves by the divergent circulation of recurving tropical cyclones. *J. Atmos. Sci.*, **67**, 3600–3616, doi:10.1175/2010JAS3459.1.

Hoskins, B. J., I. Draghici, and H. C. Davies, 1978: A new look at the ω-equation. *Quart. J. Roy. Meteor. Soc.*, **104**, 31–38, doi:10.1256/smsqj.43902.

——, M. McIntyre, and A. W. Robertson, 1985: On the use and significance of isentropic potential vorticity maps. *Quart. J. Roy. Meteor. Soc.*, **111**, 877–946, doi:10.1002/qj.49711147002.

Jones, S. C., and Coauthors, 2003: The extratropical transition of tropical cyclones: Forecast challenges, current understanding, and future directions. *Wea. Forecasting*, **18**, 1052–1092, doi:10.1175/1520-0434(2003)018<1052:TETOTC>2.0.CO;2.

Keller, J. H., S. C. Jones, and P. A. Harr, 2014: An eddy kinetic energy view of physical and dynamical processes in distinct forecast scenarios for the extratropical transition of two tropical cyclones. *Mon. Wea. Rev.*, **142**, 2751–2771, doi:10.1175/MWR-D-13-00219.1.

Kitabatake, N., 2008: Extratropical transition of tropical cyclones in the western North Pacific: Their frontal evolution. *Mon. Wea. Rev.*, **136**, 2066–2090, doi:10.1175/2007MWR1958.1.

Klein, P. M., P. A. Harr, and R. L. Elsberry, 2002: Extratropical transition of western North Pacific tropical cyclones: Midlatitude and tropical cyclone contributions to reintensification. *Mon. Wea. Rev.*, **130**, 2240–2259, doi:10.1175/1520-0493(2002)130<2240:ETOWNP>2.0.CO;2.

Knapp, K. R., M. C. Kruk, D. H. Levinson, H. J. Diamond, and C. J. Neumann, 2010: The International Best Track Archive for Climate Stewardship (IBTrACS). *Bull. Amer. Meteor. Soc.*, **91**, 363–376, doi:10.1175/2009BAMS2755.1.

Martius, O., C. Schwierz, and H. C. Davies, 2008: Far-upstream precursors of heavy precipitation events on the Alpine southside. *Quart. J. Roy. Meteor. Soc.*, **134**, 417–428, doi:10.1002/qj.229.

McTaggart-Cowan, R., L. F. Bosart, J. R. Gyakum, and E. H. Atallah, 2007: Hurricane Katrina (2005). Part II: Evolution and hemispheric impacts of a diabatically generated warm pool. *Mon. Wea. Rev.*, **135**, 3927–3949, doi:10.1175/2007MWR2096.1.

Moore, J. T., and G. E. Vanknowe, 1992: The effect of jet-streak curvature on kinematic fields. *Mon. Wea. Rev.*, **120**, 2429–2441, doi:10.1175/1520-0493(1992)120<2429:TEOJSC>2.0.CO;2.

Nieto Ferreira, R., and W. H. Schubert, 1999: The role of tropical cyclones in the formation of tropical upper-tropospheric troughs. *J. Atmos. Sci.*, **56**, 2891–2907, doi:10.1175/1520-0469(1999)056<2891:TROTCI>2.0.CO;2.

Orlanski, I., and J. P. Sheldon, 1995: Stages in the energetics of baroclinic systems. *Tellus*, **47A**, 605–628, doi:10.1034/j.1600-0870.1995.00108.x.

Pantillon, F., J.-P. Chaboureau, C. Lac, and P. Mascart, 2013: On the role of a Rossby wave train during the extratropical transition of Hurricane Helene (2006). *Quart. J. Roy. Meteor. Soc.*, **139**, 370–386, doi:10.1002/qj.1974.

——, ——, and E. Richard, 2015: Remote impact of North Atlantic hurricanes on the Mediterranean during episodes of intense rainfall in autumn 2012. *Quart. J. Roy. Meteor. Soc.*, **141**, 967–978, doi:10.1002/qj.2419.

Parker, T. J., G. J. Berry, and M. J. Reeder, 2013: The influence of tropical cyclones on heat waves in Southeastern Australia. *Geophys. Res. Lett.*, **40**, 6264–6270, doi:10.1002/2013GL058257.

Reynolds, C. A., M. S. Peng, and J.-H. Chen, 2009: Recurving tropical cyclones: Singular vector sensitivity and downstream impacts. *Mon. Wea. Rev.*, **137**, 1320–1337, doi:10.1175/2008MWR2652.1.

Riemer, M., and S. C. Jones, 2010: The downstream impact of tropical cyclones on a developing baroclinic wave in idealized scenarios of extratropical transition. *Quart. J. Roy. Meteor. Soc.*, **136**, 617–637, doi:10.1002/qj.605.

——, and ——, 2014: Interaction of a tropical cyclone with a high-amplitude, midlatitude wave pattern: Waviness analysis, trough deformation and track bifurcation. *Quart. J. Roy. Meteor. Soc.*, **140**, 1362–1376, doi:10.1002/qj.2221.

——, ——, and C. A. Davis, 2008: The impact of extratropical transition on the downstream flow: An idealized modelling study with a straight jet. *Quart. J. Roy. Meteor. Soc.*, **134**, 69–91, doi:10.1002/qj.189.

——, M. Baumgart, and S. Eiermann, 2014: Cyclogenesis downstream of extratropical transition analyzed by Q-vector partitioning based on flow geometry. *J. Atmos. Sci.*, **71**, 4204–4220, doi:10.1175/JAS-D-14-0023.1.

Ritchie, E. A., and R. L. Elsberry, 2007: Simulations of the extratropical transition of tropical cyclones: Phasing between the upper-level trough and tropical cyclones. *Mon. Wea. Rev.*, **135**, 862–876, doi:10.1175/MWR3303.1.

Rodwell, M. J., and Coauthors, 2013: Characteristics of occasional poor medium-range weather forecasts for Europe. *Bull. Amer. Meteor. Soc.*, **94**, 1393–1405, doi:10.1175/BAMS-D-12-00099.1.

Scheck, L., S. C. Jones, and M. Juckes, 2011a: The resonant interaction of a tropical cyclone and a tropopause front in a barotropic model. Part I: Zonally oriented front. *J. Atmos. Sci.*, **68**, 405–419, doi:10.1175/2010JAS3482.1.

——, ——, and ——, 2011b: The resonant interaction of a tropical cyclone and a tropopause front in a barotropic model. Part II: Frontal waves. *J. Atmos. Sci.*, **68**, 420–429, doi:10.1175/2010JAS3483.1.

Scherrer, S. C., M. Croci-Maspoli, C. Schwierz, and C. Appenzeller, 2006: Two-dimensional indices of atmospheric blocking and their statistical relationship with winter climate patterns in the Euro-Atlantic region. *Int. J. Climatol.*, **26**, 233–249, doi:10.1002/joc.1250.

Souders, M. B., B. A. Colle, and E. K. M. Chang, 2014: The climatology and characteristics of Rossby wave packets using a feature-based tracking technique. *Mon. Wea. Rev.*, **142**, 3528–3548, doi:10.1175/MWR-D-13-00371.1.

Torn, R. D., 2010: Diagnosis of the downstream ridging associated with extratropical transition using short-term

ensemble forecasts. *J. Atmos. Sci.*, **67**, 817–833, doi:10.1175/2009JAS3093.1.

——, and G. J. Hakim, 2015: Comparison of wave packets associated with extratropical transition and winter cyclones. *Mon. Wea. Rev.*, **143**, 1782–1803, doi:10.1175/MWR-D-14-00006.1.

——, J. S. Whitaker, P. Pegion, T. M. Hamill, and G. J. Hakim, 2015: Diagnosis of the source of GFS medium-range track errors in Hurricane Sandy (2012). *Mon. Wea. Rev.*, **143**, 132–152, doi:10.1175/MWR-D-14-00086.1.

Wirth, V., and J. Eichhorn, 2014: Long-lived Rossby wave trains as precursors to strong winter cyclones over Europe. *Quart. J. Roy. Meteor. Soc.*, **140**, 729–737, doi:10.1002/qj.2191.

Zimin, A. V., I. Szunyogh, D. J. Patil, B. R. Hunt, and E. Ott, 2003: Extracting envelopes of Rossby wave packets. *Mon. Wea. Rev.*, **131**, 1011–1017, doi:10.1175/1520-0493(2003)131<1011:EEORWP>2.0.CO;2.

——, ——, B. R. Hunt, and E. Ott, 2006: Extracting envelopes of nonzonally propagating Rossby wave packets. *Mon. Wea. Rev.*, **134**, 1329–1333, doi:10.1175/MWR3122.1.